The Role of Soil Moisture in Land-Atmosphere Interactions

A Study using Large Eddy Simulations and the Tiled ECMWF Scheme for Surface Exchanges over Land

by

M.P. van Soest

to obtain the degree of Master of Science
MSc. Climate Physics

Supervisors:
Dr. ir. Remco Verzijlbergh
Dr. Michiel Baatsen
2nd examinor: Dr. Anna von der Heydt

Utrecht University

whiffle
precision weather forecasting

Student number: 5327865
February 6, 2023

Acknowledgements

The finalization of this thesis marks the end of my time in the Master programme Climate Physics at University Utrecht and thereby also the end of my time as a student. After finishing my bachelor degree Applied Physics at TU Delft in 2020, I realized I wanted to narrow my studies and really focus on what I found the most interesting: the weather. Soon after moving to Utrecht I realized this was the best choice I could have made, since the courses were interesting and I met amazing people who shared my interests. For my thesis I decided to take a small step outside the university and I am very happy I found my way to Whiffle.

In the past 6 months, I divided my time between the master student room in the Buys Ballot building and Whiffle's office in Delft. It was always a nice change to go from fellow students dealing with the same challenges to the atmosphere at Whiffle and back again. This also meant I had the advantage of two supervisors that were both always available for guidance. I would like to thank Michiel Baatsen for supervising this thesis with enthusiasm, sharing all his knowledge and pushing me to find the root answers to my questions. I also thank Remco Verzijlbergh who supervised this project with a lot of attention and helped narrow down the research and push me to come up with a clear and convincing story.

I would like to thank the rest of the people at Whiffle too for making me feel like part of the company, not only by showing an interest in my work but also during the hours spent climbing in the bouldering gym. A special thanks goes to Evert Wiegant who answered all of my daily questions and was ready to dive into spreadsheets of statistics with me to find the answers I was looking for.

Writing a thesis is a massive challenge and I am convinced it would have been a lot harder without my fellow students and friends Raeven en Jan who spent many hours and lunches with me in Utrecht and were always able to take the thesis frustrations away. Lastly, I thank Tijmen for cheering me up during the stressful times and my family and friends for their support during my full student period.

Abstract

Soil moisture plays a crucial role in land-atmosphere interactions through its ability to divide the incoming radiation into latent heating and sensible heating. Accurate modelling of soil moisture could significantly improve numerical weather prediction, but observational data is difficult to obtain. In this research, the Tiled ECMWF Scheme for Surface Exchanges over Land (TESSEL) is coupled to Whiffle's large eddy simulation model called GRASP and the behaviour of this system is explored. It is concluded that TESSEL is highly sensitive to initial conditions of soil moisture and soil parameters. In 6 months of model runs, rain-soil moisture coupling improves the model results through increased latent heating. Differentiation between soil types in Cabauw and Gilze-Rijen also increases the model skills, concluded from decreased biases and increased correlations with observations of surface fluxes, temperature, humidity and wind speed. This effect is strongest in summer and also influences wind speed and cloud formation. In a radiation fog case study, initialization with atmospheric observations produced a fog layer close to observations in depth, with the dissipation delayed by an hour. For this model set-up, it is recommended to permanently add differentiation between soil types, so that the initial soil moisture matches the soil parameters. Some improvements made to TESSEL should be added such as the conductivity formulation, the bare soil evaporation and the addition of surface run-off. In future research the behaviour of the system during heavy rainfall could be studied, as well as the influence of open boundary conditions and the use of other data sources for initialization.

Contents

1 Introduction

Land surfaces and the atmosphere interact in complex and non-linear ways, on timescales ranging from seconds to years. The moisture present in the top layers of the soil plays an important role in the coupling between land and atmosphere, by affecting the evaporation from the surface. This indirectly links soil moisture to cloud formation, precipitation, near-surface temperatures [Hirschi et al., 2011] and fog formation [Bergot and Guedalia, 1994] [Guedalia and Bergot, 1994]. Soil moisture has a memory that can last months [Seneviratne et al., 2006], which means deviations on seasonal timescales have a large effect on weather prediction. For example, spring soil moisture conditions can greatly influence the development of heat waves in summer [Fischer et al., 2007]. As climate change is causing more extreme droughts and higher chances of flooding [Grillakis, 2019] [Seneviratne et al., 2010], an accurate representation of the land-atmosphere coupling becomes increasingly critical. Beyond the impact soil moisture has on the atmosphere, an accurately estimation is also essential in the field of water management, food production, water quality, and safety.

Land-atmosphere interactions

The interaction between the surface and the atmosphere, combined with the diurnal cycle of radiation, forms a complex system consisting of multiple feedback loops. The most important aspects for this research are shown in figure 1.1.

The energy source that drives the atmospheric dynamics is the sun, which provides energy to the earth surface. The soil moisture plays a part in determining how this energy is used, which is either for latent heating (evaporation) or sensible heating (increasing temperature). This division of energy, quantified by the Bowen ratio, therefore makes the atmosphere either more humid or warmer. The temperature and humidity in the atmosphere cause a wide range of effects like increasing the boundary layer height and causing cloud formation and rain. The wind speed is also affected through the drag at the top of the boundary layer and the stratification strength and lastly, the diurnal cycle of the radiation can cause radiation fog, which depends on the temperature and humidity at night.

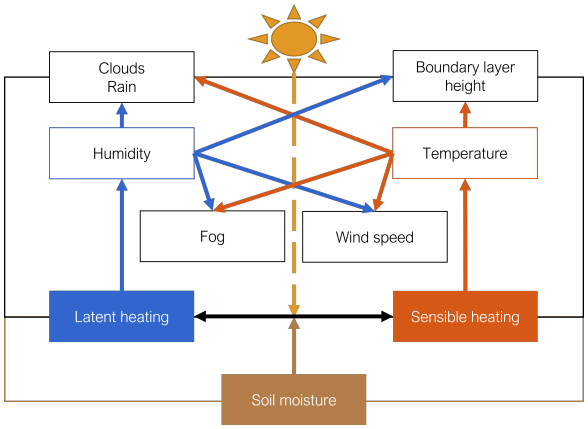

Figure 1.1: *Schematic of the influence of soil moisture on the boundary layer.*

These processes give a rough picture of the land-atmosphere interaction but are determined by many factors such as surface properties: vegetation and soil type, soil temperature, vegetation structure and the state of the free troposphere, which can be influenced by large scale atmospheric processes. Koster et al. [2004a] showed that the strength of land-atmosphere coupling is largely dependant on location by comparing outputs from a dozen models. Their results showed that this coupling is strongest in transition zones between wet and dry climates.

Soil moisture data

Most weather prediction models and general circulation models use intricate sub-surface schemes that take into account processes like dew collection, surface runoff, and water extraction by plant roots. The current challenge is a lack of observational data to feed these models for initial conditions and validation. Studies have shown that using observational data to initialize the sub-surface scheme in weather models results in significantly improved forecasts, particularly during the summer (Ardilouze et al. [2017], Koster et al. [2004b]). While there are individual locations where soil is sampled or continuously measured, the spatial variability in soil moisture can be high and measurement techniques are susceptible to various factors and disagree on the type of soil moisture measured [SU et al., 2014].

Another approach for obtaining soil moisture measurement is remote sensing. There are two primary remote sensing products that provide soil moisture data. The European Space Agency (ESA) launched the Soil Moisture Ocean Salinity (SMOS) mission in 2009, with a 35-50 km resolution and a temporal revisit of 3 days. The Soil Moisture Active Passive (SMAP) mission was launched in 2015 by NASA, which has a spatial and temporal resolution similar to SMOS (35 km, 3 days). SMOS uses a passive microwave radiometer, while SMAP has both a passive radiometer and an active radar that are combined. Microwave radiometers allow soil moisture to be observed under all weather conditions, including rain and clouds. Vegetation influences are minimized by using L-band frequencies (low, 1-2 GHz). The output of these instruments is used in algorithms that calculate soil moisture, but only for the top 5 cm of the ground [Das et al., 2010]. Burgin et al. [2017] compared the two products with several others and concluded that SMAP and SMOS were very similar, with SMOS providing slightly higher soil moisture values than SMAP. Mohanty et al. [2017] noted that the algorithms used do not work optimally in heterogeneous landscapes and that the calculated soil moisture is sensitive to several other properties (e.g. roughness, vegetation water content)

The data retrieved from remote sensing is used in many studies to obtain soil moisture data with higher resolutions and in deeper soil layers. Das et al. [2010] developed an algorithm that combines the data from the passive and active SMAP instruments and produces 9 km resolution soil moisture data. This output has been used by many others to obtain even higher resolutions.

For example, Fang et al. [2020] used a downscaling algorithm based on thermal inertia theory to convert the 9 km SMAP soil moisture data to 1 km resolution. They used surface skin temperature and soil moisture measurements to build a model, which is then used to convert the SMAP soil moisture to a 1 km resolution grid. The results showed improved correlation with observations, and maps showed smaller scale features not present in the original SMAP data. Lee et al. [2019] calculated soil moisture at 4 km resolution in the Korean Peninsula using satellite observations of energy fluxes, mass fluxes, and vegetation properties combined with in situ-measurements of precipitation, 2 m air temperature, humidity, soil moisture, elevation and slope information. All this data was fed into a deep neural network to build a soil moisture estimation model. The trained model achieved a high correlation (> 0.87) and low RMSE ($<4.15\%$).

Set-up and questions

The sub-surface scheme used in this study is the Tiled ECMWF Scheme for Surface Exchanges over Land (TESSEL) [Viterbo and Beljaars, 1995], an extensive model that includes four soil layers and surface flux parameterizations, depending on the tile type. This scheme has been tested with observations in various studies using datasets from around the world (van den Hurk et al. [2000], Gustafsson et al. [2003], Balsamo et al. [2009]). Over the years, some important modifications were done, like the revision of the hydraulic properties to accommodate different soil types, the enhancement of runoff, the addition of variable leaf area index (LAI) [Boussetta et al., 2013], and the change of bare soil evaporation in dry conditions [Balsamo et al., 2011].

While all the research mentioned above has used global or regional weather forecasting models, this study uses Large Eddy Simulations (LES) that are coupled to the ERA5 re-analysis data and the TESSEL scheme. The model used is called GRASP and was provided by Whiffle, a scale-up company based in Delft that produces precision weather forecasting. LES models can produce high resolution results while resolving turbulence close

to the surface. Since the TESSEL scheme was created for ECMWF's Integrated Forecasting System (IFS) [ECMWF, 2020], the main focus of this research is to investigate how this scheme behaves when coupled to an LES model such as GRASP, to see what capabilities it has in predicting several weather phenomena and to identify improvements. The research questions are formulated as follows:

1. How does TESSEL capture the role of soil moisture in land-atmosphere interactions?
2. Does rain-soil moisture coupling and soil type differentiation improve modelling skills in LES runs?
3. How accurately is radiation fog reproduced and how can this be improved?

A description of the LES model GRASP and TESSEL is given in section 2, which will answer question 1 theoretically. An overview of the data used in this research is given in section 3. The rest of this report consists of 3 parts each containing a set-up section and results. Question 1 is further answered with a sensitivity analysis in section 4. A large amount of model runs are used to answer question 2 in section 5 and a case-study of radiation fog is presented to answer question 3 in section 6. Finally, conclusions of all the results are drawn in section 7, and recommendations and an outlook are given in section 8.

2 Model Description

2.1 GRASP

The LES model used in this study is the GPU-Resident Atmospheric Simulation Platform (GRASP), provided by Whiffle. The most important equations in the model are described here. As this model is closely related to the Dutch Atmospheric Large-Eddy Simulation (DALES), for a detailed description Heus et al. [2010] and Schalkwijk et al. [2015] can be consulted.

2.1.1 Governing equations

In general, atmospheric models solve the equations of motion, consisting of conservation equations for mass, momentum and scalar variables. LES models are set apart by their ability to resolve turbulence where large-scale models fully parameterize it. Before solving the equations of motion, a spatial filter is applied to the prognostic variables resulting in a resolved part and a subgrid part. This subgrid part of the variables is solved using an eddy-viscosity model, while the resolved part enters the equations of motion given below.

In GRASP, a reference density profile $\rho_b(z)$ is used following from the anelastic approximation [Böing et al., 2012]. The equations of motion after LES filtering then become

$$\frac{\partial \rho_b(z) u_j}{\partial x_j} = 0, \tag{2.1}$$

$$\rho_b \frac{\partial u_i}{\partial t} = -\frac{\partial \rho_b u_i u_j}{\partial x_j} - \frac{\partial p}{\partial x_i} + \rho_b b \delta_{i3} + f_i - \frac{\partial \tau_{ij}}{\partial x_j} + \epsilon_{ij3} f_c (u_j - u_j^g), \tag{2.2}$$

$$\rho_b \frac{\partial \phi}{\partial t} = \frac{\partial \rho_b u_j \phi}{\partial x_j} - \frac{\partial F_j^q}{\partial x_j} + S_\phi. \tag{2.3}$$

Here u_j denotes the LES-filtered velocities in x,y,z direction. p is the pressure, b is a representation of the buoyancy, δ_{i3} is the Kronecker delta, f_i represent external forcing, τ_{ij} is the subgrid-stress tensor, ϵ_{ij3} is the Levi-Civita symbol, f_c is the Coriolis parameter and u_j^g are the components of the geostrophic wind.

In equation 2.3, ϕ denotes a prognostic variable, F_j^ϕ its subgrid fluxes and S_ϕ its local sources and sinks. The prognostic variables governed by this equation are $\{u, v, q_t, \theta_l\}$. The latter two are the total specific humidity and a temperature derived from liquid/ice static energy, thermodynamic variables that are conserved under water phase changes. The total specific humidity consists of the mixing ratio's of water vapor q_v, liquid water q_l and ice q_i:

$$q_t = q_v + q_l + q_i. \tag{2.4}$$

The temperature derived from liquid/ice static energy can be written as

$$\theta_l = -T_0 + T + \frac{g}{c_p} z - \frac{L_v}{c_p} q_l - \frac{L_i}{c_p} q_i, \tag{2.5}$$

where $(T - T_0)$ is the temperature in Celsius, g is the gravitational acceleration, c_p is the specific heat of water and L_v, L_i are the latent heat of vaporization and sublimation, respectively.

Integration The governing equations are numerically integrated in GRASP using a third order Runge-Kutta scheme. The timestep is determined during runtime so that the Courant–Friedrichs–Lewy condition is met as follows:

$$\Delta t = \min\left(\Delta t_{max}, C \min\left(\frac{\Delta x_i}{u_i}\right)\right). \tag{2.6}$$

Δt_{max} is set to 20 seconds, Δx_i is the grid cell size in the direction of the largest velocity and C is the Courant number, which is set to 0.8.

Advection is discretized using the flux-form, where the prognostic variables are approximated using a second order central difference scheme.

2.1.2 Model boundary conditions

In all runs in this study, periodic boundary conditions are used for the sides of the domain. At the top of the domain, following boundary conditions are used:

$$\frac{\partial u}{\partial z} = \frac{\partial v}{\partial z} = 0, \tag{2.7a}$$

$$w = 0, \tag{2.7b}$$

$$\frac{\partial \phi}{\partial z} = c_\phi, \tag{2.7c}$$

where c_ϕ is a constant set per run and per variable.

2.1.3 Large-scale coupling

The source term S_ϕ in equation 2.3 consists of three parts set by large-scale conditions. These large-scale conditions, as well as the initial conditions, can be taken from large-scale products such as the ERA5 reanalysis or input profiles can be provided. The first source/sink term is the subsidence W, which enters the source term as

$$S_\phi^{sub} = -W\frac{\partial \phi}{\partial z}. \tag{2.8}$$

Secondly, large-scale advection is added as

$$S_\phi^{adv} = U\frac{\partial \Phi}{\partial x} + V\frac{\partial \Phi}{\partial y}, \tag{2.9}$$

where U, V, Φ are the large-scale variables.

These large-scale variables can also be nudged towards during the run, by adding the final source term, called 'relaxation', which scales with the difference between the large scale variable and the horizontally averaged LES variable $\overline{\phi}$ as

$$S_\phi^{rel} = -\frac{1}{\tau}\Big(\overline{\phi} - \Phi\Big). \tag{2.10}$$

This can be done at different heights in the domain and the strength is controlled by the time-scale parameter τ.

2.2 TESSEL

The Tiled ECMWF Scheme for Surface Exchanges over Land (TESSEL) was first introduced by Viterbo and Beljaars [1995] to solve several problems that were found in the ECMWF's forecasts at the time:

- Too much evaporation in wet conditions and too little evaporation in dry conditions
- A large positive bias in surface temperature in summer daytime
- Inaccuracies in the land hydrology

The first version of this model was kept simple, using a single type of soil and vegetation. The model consists of four soil layers with varying depths (7 cm, 21 cm, 72 cm, 189 cm), and different types of tiles at the surface. In the first model proposed there were three tile possibilities: bare soil, vegetation and an interception reservoir. Some years later, the vegetation was split into low and high vegetation and snow-covered land was added.

A revised TESSEL scheme (H-TESSEL) was introduced by Balsamo et al. [2009], in which soil types are varied spatially, the soil hydraulic properties were improved and the surface runoff term was refined to be dependent on soil type and topography. ECMWF [2020] documents that the runoff is a significant feature that can vary between 1% to 50% of the rainfall.

The top boundary condition for heat is determined by a zero-depth skin layer that exchanges energy with the atmosphere and the top soil layer. The top boundary condition for water is determined separately for the various tiles and the lower boundary condition is free drainage.

2.2.1 Soil heat and moisture processes

Soil heat transport

Heat is transported between the soil layers following Fourier's law of diffusion, which gives the heat flux F_T as a function of the soil heat conductivity λ_T and the vertical temperature gradient, which is defined positive downwards.

$$F_T = -\lambda_T\frac{\partial T}{\partial z}. \tag{2.11}$$

This heat flux results in local heating within the soil layers to maintain conservation of energy. The temperature change in time thus depends on the vertical gradient of the heat flux, given by the differential equation

$$\frac{\partial T}{\partial t} = \frac{1}{(\rho C)_s}\frac{\partial}{\partial z}\Big(\lambda_T\frac{\partial T}{\partial z}\Big), \tag{2.12}$$

with $(\rho C)_s$ the soil heat capacity which is parameterized, following Johansen [1977], as

$$(\rho C)_s = (1 - q_{s,sat})(\rho C)_{dry} + q_s(\rho C)_{water}. \tag{2.13}$$

$(\rho C)_{dry}, (\rho C)_{water}$ are the heat capacities of dry soil and water, respectively.

The heat conductivity is parameterized according to Peters-Lidard et al. [1998]:

$$\lambda_T = \mathrm{Ke}(\lambda_{T,sat} - \lambda_{T,dry}) + \lambda_{T,dry}, \tag{2.14}$$

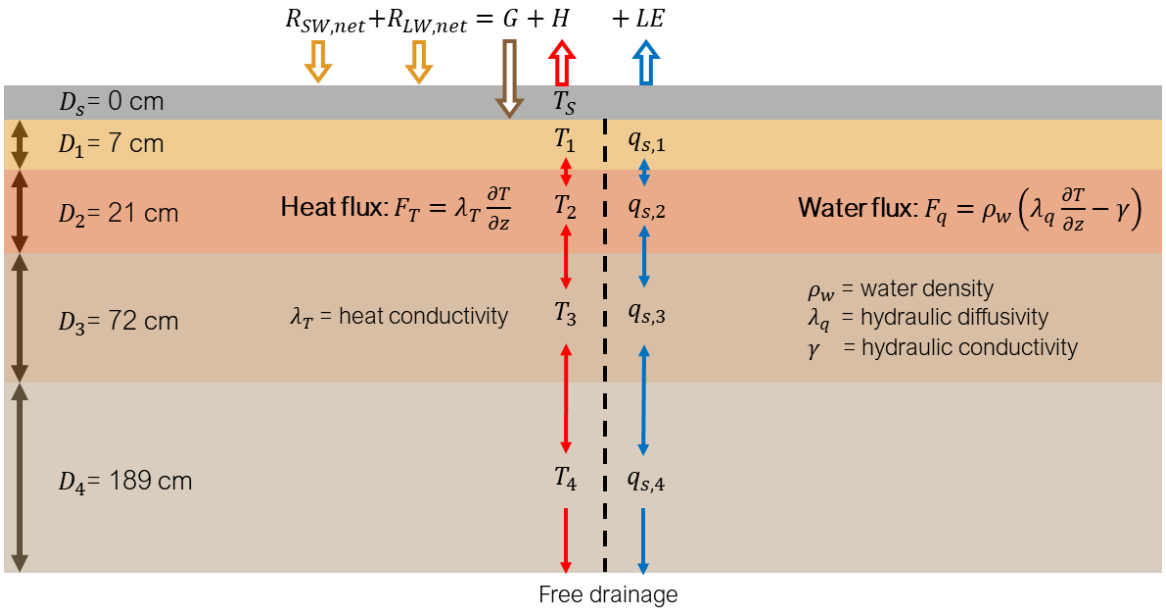

Figure 2.1: *Schematic of the soil moisture and heat processes in TESSEL.*

where Ke is the Kersten number:

$$\text{Ke} = \log_{10}\left(\max\left(0.1, \frac{q_s}{q_{s,sat}}\right)\right) + 1. \tag{2.15}$$

$\lambda_{T,sat}, \lambda_{T,dry}$ are the heat conductivity's of saturated soil and dry soil, respectively. The saturated soil conductivity is given by

$$\lambda_{T,sat} = \lambda_{T,s}^{1-q_s} \lambda_{T,water}^{q_s}, \tag{2.16}$$

with $\lambda_{T,s}$ the soil solids thermal conductivity and $\lambda_{T,water}$ is the heat conductivity of water.

Soil water transport

The water flux between the soil layers is calculated using Darcy's law:

$$F_w = -\rho_w\left(\lambda_q \frac{\partial q_s}{\partial z} - \gamma\right), \tag{2.17}$$

where ρ_w is the water density at room temperature, λ_q is the hydraulic diffusivity and γ is the hydraulic conductivity.

The change in soil moisture content in time within the layers is calculated as

$$\rho_w \frac{\partial q_s}{\partial t} = -\frac{\partial F_w}{\partial z} + \rho_w S_{q_s}, \tag{2.18}$$

where the volumetric water content q_s change depends on the gradient of F_w and S_{q_s}, the root water uptake. Equation 2.17 can be substituted to find a partial differential equation for q_s:

$$\frac{\partial q_s}{\partial t} = \frac{\partial}{\partial z}\left(\lambda_q \frac{\partial q_s}{\partial z} - \gamma\right) + S_{q_s}. \tag{2.19}$$

The hydraulic diffusivity and conductivity, λ_q and γ, are function of the soil water content. Several formulations for these variables can be found in literature. The original TESSEL scheme uses the Clapp and Hornberger [1978] formulations:

$$\gamma = \gamma_{sat}\left(\frac{q_s}{q_{s,sat}}\right)^{2b_c+3} \tag{2.20a}$$

$$\lambda_q = \frac{b_c \gamma_{sat}(-\psi_{sat})}{q_{s,sat}}\left(\frac{q_s}{q_{s,sat}}\right)^{b_c+2}, \tag{2.20b}$$

with constants $\gamma_{sat} = 0.57e-6$ m/s, $b_c = 6.04$ and $\psi_{sat} = -0.338$ m.

In H-TESSEL one of the extensions was the differentiation between soil types. Therefore the Clapp and Hornberger conductivity formulation was replaced by Van Genuchten [1980]:

$$\gamma = \gamma_{sat}\frac{\left((1+\alpha h^2)^{1-1/n} - \alpha h^{n-1}\right)^2}{(1+\alpha h^n)^{(1-1/n)(l+2)}}, \tag{2.21}$$

where α, n, l are soil-dependent parameters. h is the

pressure head, which is in turn linked to soil moisture as

$$q_s(h) = q_{s,r} + \frac{q_{s,sat} - q_{s,r}}{(1+\alpha h)^{(1-1/n)}}. \tag{2.22}$$

The root extraction is per soil layer k using

$$S_{q_s,k} = \frac{R_k q_{s,k}}{\sum_{j=1}^{4} R_j q_{s,j}} c_v L E_v, \tag{2.23}$$

where the vegetation evaporation E_v, the coverage c_v and the root fraction R_k all will be defined later in this section. The sum over j is a sum over soil layers.

2.2.2 Boundary conditions

Surface energy balance

The top boundary condition for the heat transfer equations is the energy balance in the skin layer, which has zero thickness and therefore cannot store heat. The surface energy balance becomes

$$R_{SW,net} + R_{LW,net} - H - LE - G = 0, \tag{2.24}$$

where $R_{SW,net}, R_{LW,net}$ are the short wave and long wave net radiation, respectively. H is the sensible heat flux, LE is the latent heat flux and G is the ground heat flux going into the first soil layer, all in [W/m^2]. The net radiation fluxes are calculated using the albedo α, the Stefan-Boltzmann constant σ and and the surface emissivity ϵ and the temperature of the skin layer T_{sk}:

$$R_{SW,net} = (1-\alpha) R_{SW\downarrow} \tag{2.25}$$

$$R_{LW,net} = \epsilon\Big(R_{LW\downarrow} - \sigma T_{sk}^4\Big) \tag{2.26}$$

The ground heat flux depends on the temperature difference between the skin layer and first soil layer according to

$$G = \Lambda_{sk}\Big(T_{sk} - T_1\Big), \tag{2.27}$$

where Λ_{sk} is an empirical coefficient and T_1 is the soil temperature in the topmost layer.

The sensible heat flux is given by the Penman resistance equation:

$$H = \frac{\rho_a C_p}{r_{ah}}\Big(\theta_s - \theta_0\Big), \tag{2.28}$$

where ρ_a is the surface air density, C_p is the specific heat capacity of air, r_{ah} is the aerodynamic resistance to heat and θ_s, θ_0 are the potential temperatures of the surface and lowest atmospheric level, respectively.

The evaporation E [kg/m^2/s] is calculated seperately per tile type and added using the coverages as weights:

$$E = c_l E_l + (1-c_l) c_v E_v + (1-c_l)(1-c_v) E_s, \tag{2.29}$$

where c_v, c_l are coverages of vegetation and the liquid interception reservoir. c_v is prescribed, while c_l is calculated every timestep.

In order to calculate the total evaporation from a skin layer grid box using equation 2.29, formulations for the separate tile types are necessary.

Bare soil evaporation

The evaporation from bare soil E_s is parameterized as

$$E_s = \frac{\rho_a}{r_{aq} + r_{s,s}}\big(q_{sat} - q_0\big). \tag{2.30}$$

Here r_{aq} is the atmospheric resistance to moisture, $r_{s,s}$ is the bare soil surface resistance, q_{sat} is the saturation specific humidity at the surface, and q_0 is the specific humidity at the lowest atmospheric level.

The bare soil surface resistance depends on the soil moisture through the bare soil water stress function f_2

$$r_{s,s} = r_{s,s,min} f_{2,s}(q_{s,1}) \tag{2.31}$$

$$\frac{1}{f_{2,s}(q_{s,1})} = \begin{cases} 0, & q_{s,1} < q_{s,pwp} \\ \frac{q_{s,1} - q_{s,pwp}}{q_{s,cap} - q_{s,pwp}}, & q_{s,pwp} \le q_{s,1} \le q_{s,cap} \\ 1, & q_{s,1} > q_{s,cap} \end{cases} \tag{2.32}$$

where $q_{s,cap}$ is the field capacity soil moisture, which is the point where water does not drain from the soil by gravity anymore. $q_{s,pwp}$ is the wilting point soil moisture, which is the point where plants cannot take up water from the soil anymore and plant evaporation therefore stops. $\overline{q_s}$ is the root-averaged water content, which depends on the vegetation type.

In 2010, the wilting point water content for bare soil was lowered in IFS, resulting in lower water stress

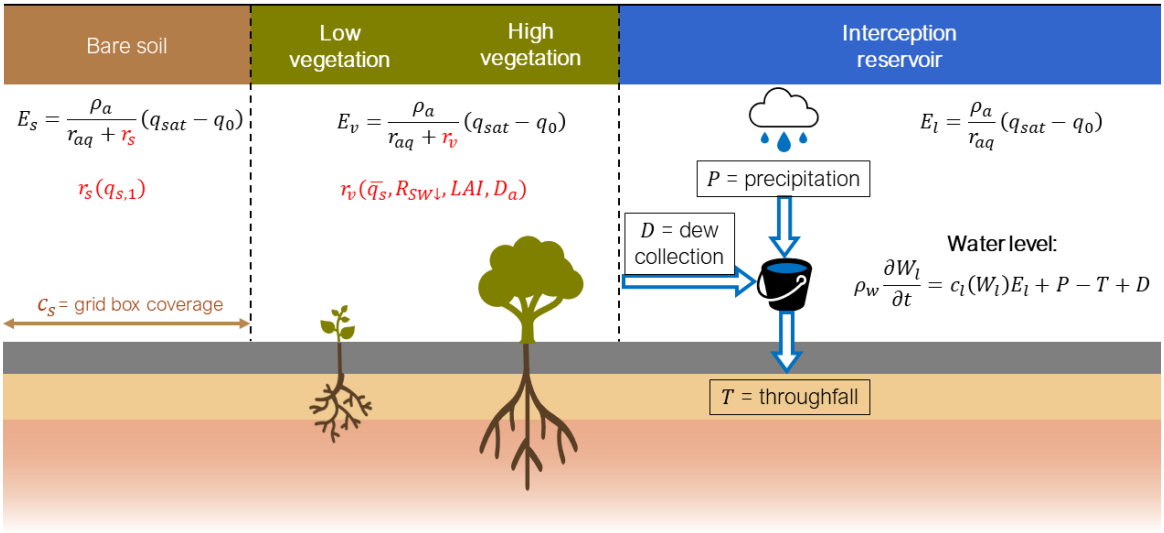

Figure 2.2: *Schematic of the water processes at the surface in TESSEL.*

and more realistic soil moisture for dry lands [Balsamo et al., 2011]. The scheme used in this study does not contain this adjustment.

Interception reservoir evaporation

The interception reservoir represents the collected water on top of the soil from precipitation and water dew. The evaporation from this reservoir is given by

$$E_l = \frac{\rho_a}{r_{aq}}(q_{sat} - q_0). \tag{2.33}$$

The coverage of the interception reservoir is variable, calculated as

$$c_l = \left(\frac{W_l}{W_{l,max}}\right), \tag{2.34}$$

with W_l the water content in the interception reservoir and $W_{l,max}$ the maximal water content. E_l, E_v, E_s are the evaporation components of the interception reservoir, vegetation and bare soil, respectively. The water content W_l, is determined every timestep by integrating

$$\rho_w \frac{\partial W_l}{\partial t} = c_l E_l + I + D, \tag{2.35}$$

where I is the interception of precipitation by the interception reservoir and D is the dew deposition from the other tiles (bare soil, high and low vegetation).

Since the interception reservoir coverage is needed for the integration of equation 2.35 but is dependant on the water level (see equation 2.34), this integration is done in three steps. First the upward evaporation is calculated by linearizing $c_l E_l$, resulting in a new value of the water level after evaporation, W_l^*:

$$\rho_w \frac{W_l^* - W_l^t}{\Delta t} = c_l(W_1^t)E_l + \frac{E_l}{W_{l,}}(W_{l,max}^* - W_l^t). \tag{2.36}$$

The evaporative flux effectively seen by the interception reservoir E_l^* is

$$E_l^* = \rho_w \frac{W_l^* - W_l^t}{\Delta t} \tag{2.37}$$

When the evaporative flux is positive (downwards), condensation takes place. For all the tiles, the dew collects in the interception reservoir until the interception reservoir is full:

$$W_l^2 = W_l^* + \min\left(W_{l,max} - W_l^*, \frac{\Delta t}{\rho_w} c_i D_i\right), \tag{2.38}$$

where D_i is the dew collection per tile i calculated as

$$D_i = \rho_w \frac{W_{l,i}^2 - W_l^*}{\Delta t}. \tag{2.39}$$

Lastly, the precipitation is partly intercepted, where the interception depends on the a factor $k = 0.5$ which is the fraction of precipitation covering the

grid box and $b_I = 0.5$ which is the interception efficiency of precipitation.

$$I = \min\left(b_I c_v P/k, \rho_w \frac{W_{l,max} - W_l^2}{\Delta t}\right) \tag{2.40}$$

The remainder of the precipitation enters the top layer of the soil as throughfall $T = P - I$.

Vegetation evaporation

The evaporation from (dry) vegetation depends on similar variables and an additional vegetation canopy resistance r_v as follows

$$E_v = \frac{\rho_a}{r_{aq} + r_v}\big(q_{sat} - q_0\big). \tag{2.41}$$

The canopy resistance was parameterized by Jarvis [1976] as

$$r_v = \frac{r_{s,min}}{LAI} f_1(R_{SW\downarrow}) f_{2,v}(\overline{q_s}) f_3(D_a), \tag{2.42}$$

where $r_{s,min}$ is the minimal stomatal resistance of a single leaf, dependent on vegetation type and LAI is the leaf area index. In 2010 a variable leaf area index over the year taken from satellite observations was added to the model, which had a positive impact on model output, especially in spring [Boussetta et al., 2013].

f_1, f_2, f_3 are vegetation stress functions, the first of which is defined as

$$\frac{1}{f_1(R_{SW\downarrow})} = \min\Big[1, \frac{bR_{SW\downarrow} + c}{a(bR_{SW\downarrow} + 1)}\Big], \tag{2.43}$$

with $a = 0.81$, $b = 0.004$ $\mathrm{W^{-1}m^2}$ and $c = 0.05$. The second stress function is inversely linear between the permanent wilting point and field capacity:

$$\frac{1}{f_{2,v}(\overline{q_s})} = \begin{cases} 0, & \overline{q_s} < q_{s,pwp} \\ \frac{\overline{q_s} - q_{s,pwp}}{q_{s,cap} - q_{s,pwp}}, & q_{s,pwp} \le \overline{q_s} \le q_{s,cap} \\ 1, & \overline{q_s} > q_{s,cap}. \end{cases} \tag{2.44}$$

Equation 2.44 is analog to equation 2.32, the only difference being the dependence not on the moisture in the top layer but on the root-averaged soil moisture $\overline{q_s}$, defined as

$$\overline{q_s} = \sum_{k=1}^{4} R_k \max\big[q_{s,k}, q_{s,pwp}\big]. \tag{2.45}$$

R_k is the root fraction which depends on vegetation-dependent parameters a_r, b_r according to Zeng et al. [1998] as

$$R_k = 0.5\big[\exp(-a_r z_{k-1/2}) + \exp(-b_r z_{k-1/2}) - \exp(-a_r z_{k+1/2}) - \exp(-b_r z_{k+1/2})\big], \tag{2.46}$$

where $z_{k+1/2}$ is the bottom of layer k.

The third stress function depends on the atmospheric humidity deficit $D_a = e_{sat} - e_L$ (e is water vapour pressure) through

$$\frac{1}{f_3(D_a)} = \exp(-g_D D_a), \tag{2.47}$$

where g_D is another parameter dependent on vegetation type.

3 Field Sites & Data

3.1 In-situ observations

Brief history on the Cabauw measurement site

Following the growing attention to air pollution in the 1950's and 1960's, the interest in boundary layer processes increased. The scientific world became more and more aware of the importance of the atmospheric boundary layer for meteorology, climate and air quality and simultaneously policy makers realized the significance of boundary layer research for aviation, construction of high rise buildings and energy production[Bosveld et al., 2020]. This led to the plan of constructing a tall measurement tower in Cabauw, able to reliably and continuously observe the boundary layer at several heights. In 1972 the tower in Cabauw was constructed and measurements started, which have gone on with few interruptions until present time [Driedonks et al., 1978].

Description of sites

The Cabauw tower is located at 51.971 °N, 4.927 °E, 0.7 m below sea level. The surroundings of the tower are agricultural, with no surface elevation higher than 20m in the vicinity [Driedonks et al., 1978]. The tall tower has instruments at 10 m, 20 m, 40 m, 80 m, 140 m and 200 m, measuring wind speed and wind direction, temperature and humidity. Beside the tall tower there are two smaller masts to measure wind close to the surface without disturbances and temperature and humidity are measured at 1.5 m height at the tall tower. In the near vicinity there are other measurement sites where surface fluxes are measured using a sonic anemometer and a H_2O/CO_2 sensor, as well as radiation (using pyraometers and purgeometers) and soil moisture (using reflectometry sensors). These measurements are done at the energy balance field close to the tall tower, shown in figure 3.1.

The other location used in this study is the KNMI measurement site in Gilze-Rijen, which is located at 51.565 °N, 4.935 °E at 14.9 m above sea level. This station measures temperature and humidity at 1.5 m height and wind speed and direction at 10 m height. Also, shortwave-down radiation and precipitation are measured there.

3.2 ECMWF re-analyses

The main data source in GRASP for the large-scale variables, initial conditions and surface variables is the ERA5 re-analysis, which contains soil moisture for all four soil layers at 31km resolution. ECMWF published a second dataset for surface variables in 2019 named ERA5-land, for which H-TESSEL is run offline using atmospheric forcing that is assimilated. This dataset has a 9km resolution and was found to be more accurate than ERA5 because it is frequently updated when the ground model is improved. Figure 3.2 shows the soil moisture time series in 2019 for the ERA5, ERA5-land datasets and the observations in Cabauw. In this location the ERA5-land dataset soil moisture is systematically about 1.2 m^3/m^3 higher, which is closer to observations especially in winter.

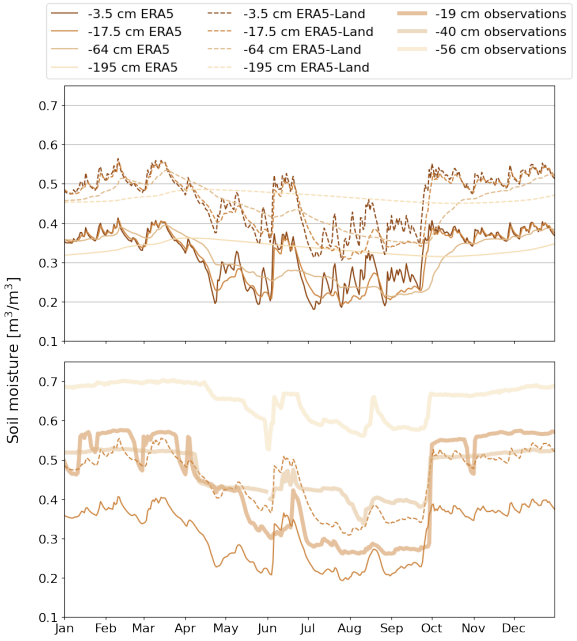

Figure 3.2: *Time series of soil moisture in 2019 from the ERA5 and ERA5-Land datasets (top) and a comparison with observations (bottom).*

(a) Cabauw

(b) Gilze-Rijen

Figure 3.1: *Satellite photo's of the measurement sites with markers for the instrument locations.*

4 Sensitivity Analysis in Idealized Conditions

In this section a sensitivity analysis is described that aims to quantify the role of soil moisture in TESSEL in idealized conditions, thereby answering the first research question. The sensitivity of the model to several soil parameters and to variations in initial soil moisture is investigated in the following set-up.

4.1 Set-up

A domain of 128x128 grid cells is used with grid cell width and length 128 m, and a stretched grid vertically starting at 32 m cell height, bringing the total domain size to 16.384 km x 16.384 km x 5 km. There are no obstacles in the domain and the land is covered homogeneously by grass. The radiation input to the surface is set to clear sky radiation at 01/06/2019 and the soil is initialized with values from the ERA5 re-analysis in Cabauw on the same day. The input profile for θ_l has a constant lapse rate of 0.5 degrees per 100 m and a surface value of 15 degrees. The input profile for q_t has a lapse rate of -0.4 in 5000 meters, starting at 0.6 g/kg at the surface. The input profile for wind is 5 m/s in x direction, constant in height. There is no subsidence or nudging, so the only term in S_ϕ is advection. A spin-up time of 1 hour is applied from 23:00, after which 24 hours are simulated.

4.2 Sensitivity to soil parameters

The soil parameters used previously by TESSEL (pre H-TESSEL) are standard input in GRASP. The values are chosen to be the approximate average of 11 soil type parameters specified in Cosby et al. [1984]. The matric potential as a function of the parameters b_c and ψ_{sat} was given by Clapp and Hornberger:

$$\psi = \psi_{sat}\left(\frac{q_s}{q_{s,sat}}\right)^{-b_c}. \tag{4.1}$$

The permanent wilting point and field capacity are defined at $\psi(q_{s,pwp}) = -15$ bar and $\psi(q_{s,cap}) = -0.33$ bar, so these values are used to find b_c and ψ_{sat} (see Jacquemin and Noilhan [1990], Hillel [2013]). In H-TESSEL, differentiation between 7 soil types added to the model. To check the effect of different soil types using the Clapp-Hornberger parameterization, b_c and ψ_{sat} are also calculated for the parameters characterizing these types. The resulting input parameters are shown in table 4.1. Note: In H-TESSEL the field capacity is defined at $\psi(q_{s,cap}) = -0.1$ bar, the values in table 4.1 are converted to -0.33 bar so they can be used in GRASP. The row labelled 'Cabauw' contains parameters from Beljaars and Bosveld [1997] who used soil measurements at the Cabauw measurement site by Jager et al. [1976] to determine the soil type as O12. From the Staring series published by Heinen et al. [2020], the parameters used in TESSEL for soil type O12 are taken.

Equations 2.20a,b are used to calculate the diffusivity and conductivity curves as a function of soil moisture. These curves are shown for the various soil types in figure 4.1.

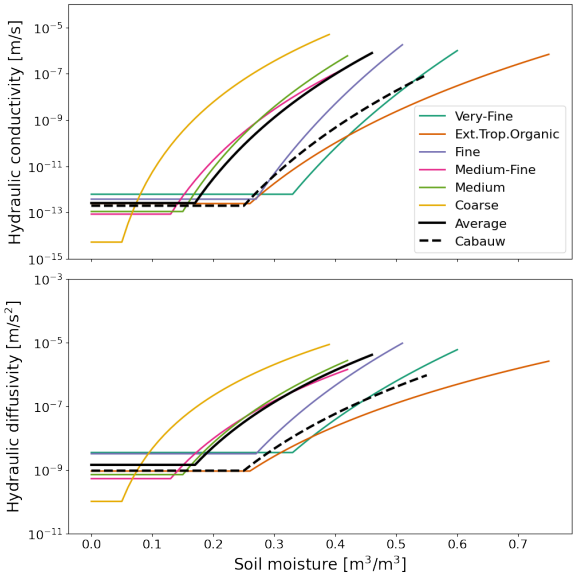

Figure 4.1: *Hydraulic conductivity and diffusivity for various soil types.*

The permanent wilting point and field capacity are also used to calculate the soil and vegetation surface resistance through the stress functions $f_{2,s}, f_{2,v}$ (see equations 2.32, 2.44). The inverse of these stress functions is shown in figure 4.2. Above field capacity, the inverse stress function is 1 which means minimal contribution to the surface resistance and no dependence on soil moisture. Below the permanent wilting point, the inverse stress function is 0 meaning infinite resistance, therefore no surface evaporation at all. Figure 4.2 therefore shows the large influence of the parameters $q_{s,pwp}, q_{s,cap}$ on the strength of the surface-atmosphere coupling.

Soil type	$\mathbf{q_{s,sat}}$ [m^3/m^3]	$\mathbf{q_{s,cap}}$ [m^3/m^3]	$\mathbf{q_{s,pwp}}$ [m^3/m^3]	$\gamma_{\mathbf{sat}}$ [10^{-6} m/s]	$\mathbf{b_c}$ [-]	$\psi_{\mathbf{sat}}$ [m]
Coarse	0.403	0.174	0.059	6.94	3.53	-0.174
Medium	0.439	0.285	0.151	1.16	6.02	-0.247
Medium-Fine	0.430	0.298	0.133	0.260	4.74	-0.589
Fine	0.520	0.400	0.279	2.87	10.6	-0.211
Very Fine	0.614	0.483	0.335	1.74	10.5	-0.272
Ext.Trop.Organic	0.766	0.534	0.267	0.930	5.51	-0.460
Average (CH)	0.472	0.323	0.171	0.570	6.00	-0.346
Cabauw	0.561	0.449	0.255	0.125	6.76	-0.599

Table 4.1: *TESSEL input parameters for various soil types specified by ECMWF [2020]. The bottom row contain parameters derived from soil measurements at Cabauw.*

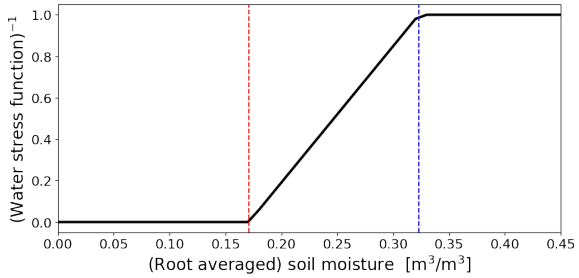

Figure 4.2: *Inverse of the water stress function for the average soil as a function of the soil moisture in the top layer (for bare soil) or the root-averaged soil moisture (for vegetation). The red dashed lines is plotted at the permanent wilting point and the blue dashed at the field capacity point.*

4.2.1 Results

Figure 4.3 shows the soil moisture in all four layers during the simulated day. A clear divide is visible in these graphs, where the coarser soils (coarse, medium, medium-fine, average) have a stronger decline in soil moisture than the fine soils (fine, ext.trop.organic, very-fine, Cabauw). This loss of moisture is a result of the heat fluxes shown in figure 4.4. The coarse soils have a higher latent heat flux than sensible heat flux, while the finer soil have almost no latent heat flux and their sensible heat flux is 3 times as high as the coarse soils. A smaller effect is also visible in the ground heat flux, showing that the fine soils will have a higher soil temperature than the coarse soils. These differences can be explained by consulting table 4.1, specifically the permanent wilting points. Since the initial soil moisture of these runs was around 0.25 m^3/m^3, the fine soils are already near or below their permanent wilting point, while the coarse soils are in the middle regime between permanent wilting point and field capacity point.

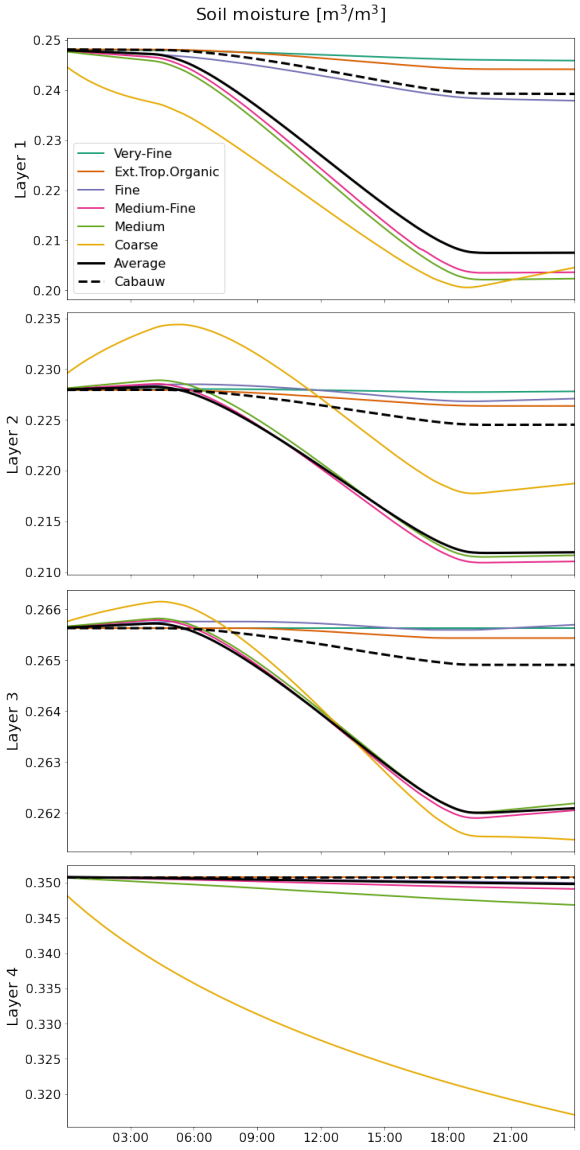

Figure 4.3: *Soil moisture in the 4 layers of TESSEL during an idealized run of a day using the soil parameters for various soil types.*

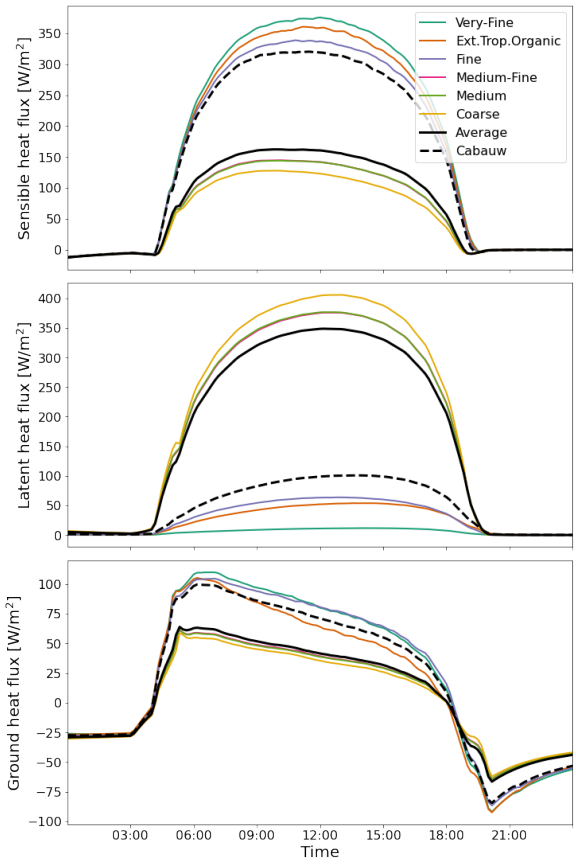

Figure 4.4: *Surface fluxes during an idealized run of a day using the soil parameters for various soil types.*

The resulting atmospheric profiles are shown in figure 4.5, at three times of day. The sensible heat flux causes a rise in temperature and the latent heat flux a rise in humidity, so these profiles are in line with the fluxes discussed above. At 6:00 the same division into fine and coarse soils is visible in the profiles, showing faster deviation from the initial profile in temperature and humidity close to the surface for the fine soils. This also results in a sharper inversion and higher boundary layer, because the higher surface heating causes stronger mixing. The surface temperature difference rises to approximately 3 degrees at noon and the boundary layer is much higher for the fine soils at that moment, as the inversion is not visible any longer for those soils. At 20:00, the low evaporation and high sensible heating in the fine soils has lead to a temperature difference of 5 degrees and a humidity difference of 4 g/kg.

4.3 Dependency on initial conditions

The initial soil moisture is varied in this section while using a single soil type. The aim of this analysis is to understand the behaviour with soil moisture above and below the permanent wilting point and field capacity. For that reason, the 'Cabauw' soil parameters are used (see table 4.1), since these have higher values for $q_{s,pwp}$ and $q_{s,cap}$. The initial soil moisture values are shown in table 4.2. The corresponding saturation soil moisture $q_{s,sat} = 0.561$ kg/kg.

4.3.1 Results

Figures 4.7 and 4.6 show the latent evaporation and atmospheric profiles at 20:00 for the runs with various initial conditions. From these graphs, it is clear how the initial conditions also have a deciding role in atmospheric conditions close to the surface. As expected from the stress function in figure 4.2, an initialization below the permanent wilting point (label PWP) causes little to no evaporation which results in a warm and dry atmosphere, with a difference of 5 degrees in temperature and 4 g/kg in specific humidity at 20:00 compared to the saturation runs. The other dry runs (labels Dry1, Dry2) have an increasing evaporation and therefore a cooler and more humid atmosphere. There is little difference between the runs that are initialized near the soil saturation. This again is expected from the stress function, since the soil in these runs has a higher moisture than the field capacity point and therefore a higher soil moisture has no influence on evaporation anymore.

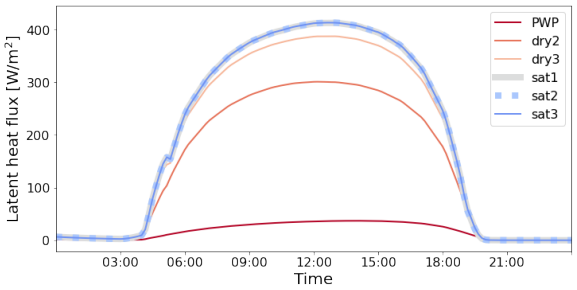

Figure 4.7: *Latent heat flux during an idealized run of a day for various soil moisture initial conditions.*

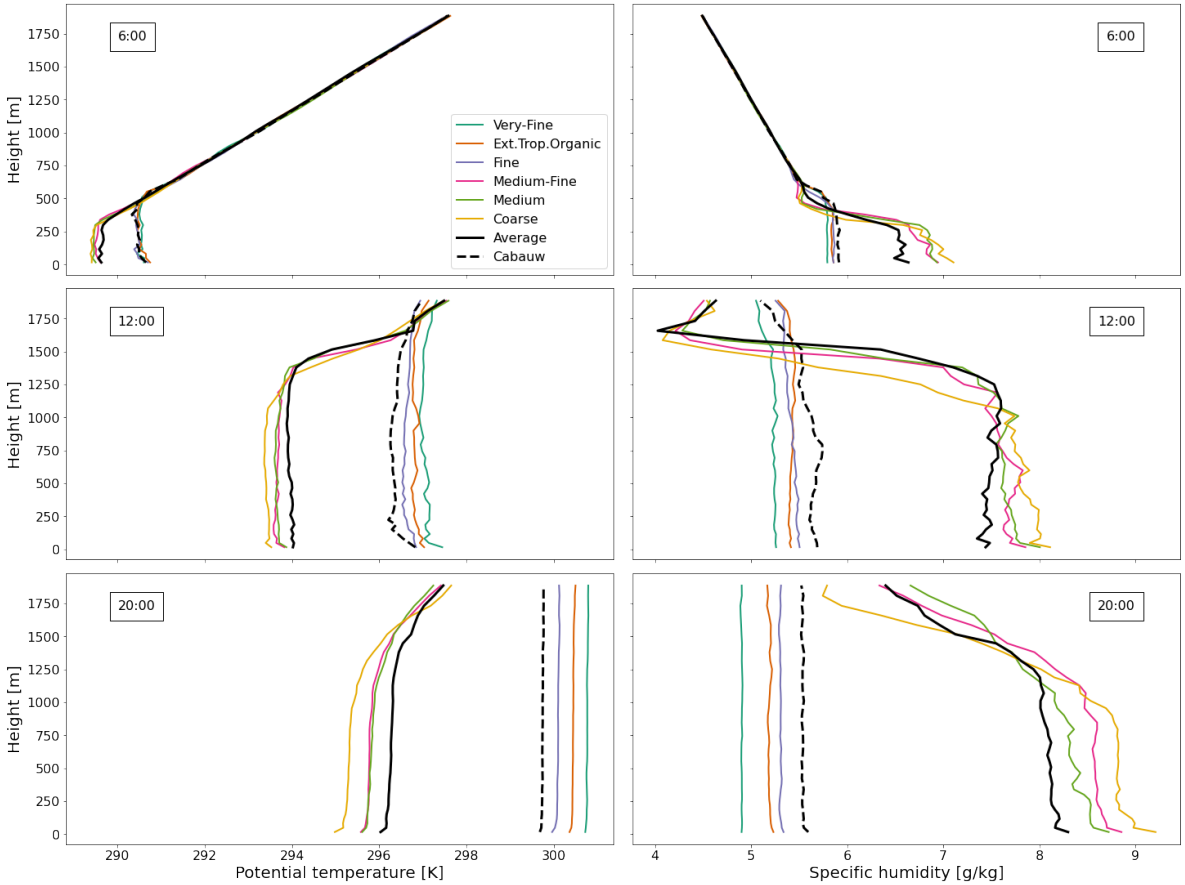

Figure 4.5: *Atmospheric profiles of potential temperature and specific humidity at three moments during an idealized run of a day for various soil settings.*

Test name	$\mathbf{q_{s,1}}$ [m^3/m^3]	$\mathbf{q_{s,2}}$ [m^3/m^3]	$\mathbf{q_{s,3}}$ [m^3/m^3]	$\mathbf{q_{s,4}}$ [m^3/m^3]	$\overline{\mathbf{q_s}}$ [m^3/m^3]
PWP	0.2	0.2	0.2	0.2	0.200
Dry1	0.3	0.3	0.35	0.4	0.378
Dry2	0.4	0.4	0.4	0.4	0.400
Sat1	$q_{s,sat}$	0.5	0.4	0.5	0.477
Sat2	$q_{s,sat}$	$q_{s,sat}$	0.4	0.5	0.481
Sat3	$q_{s,sat}$	$q_{s,sat}$	$q_{s,sat}$	$q_{s,sat}$	0.561

Table 4.2: *Test settings of soil moisture initial conditions in 4 soil layers and weighted average by layer thickness.*

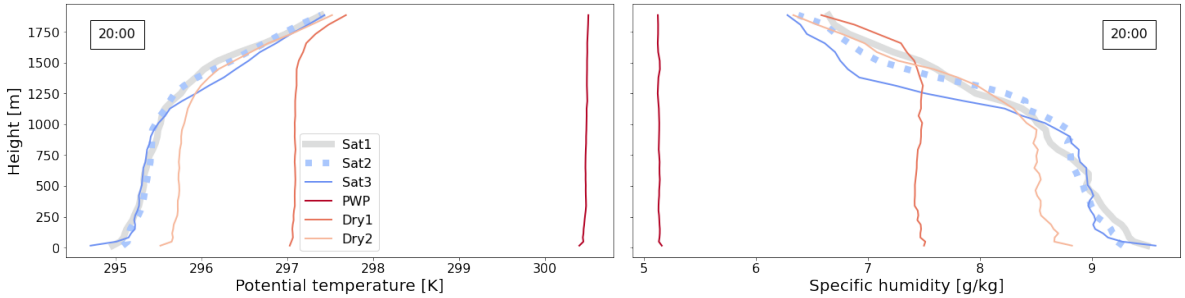

Figure 4.6: *Atmospheric profiles of potential temperature and specific humidity at 20:00 during an idealized run of a day for various soil moisture initial conditions.*

4.4 Conclusion

From these tests it can be concluded firstly that the processes happening within the soil and at the surface have a profound influence on near-surface meteorology in 'classic' LES runs with idealized input profiles and no coupling to large-scale data. In section 2.2, it was shown that the interrelation between the soil moisture and the soil parameters (especially the permanent wilting point and field capacity) determines the amount of evaporation from the soil and thereby influences the state of the near-surface atmosphere. The analysis done here using runs with various soil types and initial soil conditions confirms this mechanism, showing large differences in atmospheric conditions (5 degrees temperature and 4 g/kg humidity).

This experiment therefore shows the importance of setting the right parameters when taking initial conditions from large-scale datasets, so that they match the input initial soil moisture, because a mismatch between those two factors can cause extreme evaporation rates that strongly effect the near-surface atmosphere.

5 Rain-Soil Moisture Coupling & Soil Type Differentiation

This section is aimed answer the second research question: Does rain-soil moisture coupling and soil type differentiation improve modelling skills in LES runs? By rain-soil moisture coupling the infiltration of rain into the soil is meant, since this was turned off in the previous version of GRASP, wherein rain would disappear when reaching the surface.

5.1 Set-up

From the sensitivity analysis it was concluded that the soil parameters and particularly the permanent wilting point and field capacity can have a large influence on the atmosphere. Figure 5.1 shows the classification of soils as used by ECMWF, where large areas of sand (coarse soil) are visible in the South and East of the Netherlands. Since Cabauw is located on clay, a second location on sand was chosen, namely the KNMI weather station in Gilze-Rijen which has the record of highest temperature measured in the Netherlands. This station has one measurement height at 1.5 m where it records temperature, pressure, humidity, precipitation and wind speed every 10 minutes, but for this research hourly averages are taken.

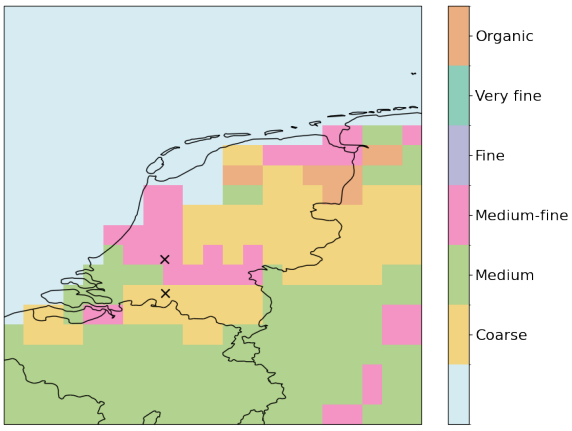

Figure 5.1: *Map of the soil types in the Netherlands as used in TESSEL by ECMWF. The crosses mark Cabauw (North) and Gilze-Rijen (South).*

Because of the near-surface measurements at 2 and 10 meter heights, a 16 m vertical resolution at the surface is used, after which the values close to the surface are interpolated. The vertical grid is stretched vertically. The horizontal resolution is set to 50 m to keep the aspect ratio of the lowest grid boxes under 4, which is required for the subgrid formulation. The simulations are done in two domain sizes:

- Small domain: 3.2 km x 3.2 km x 3.0 km
- Big domain: 6.4 km x 6.4 km x 8.0 km

As the domain is reasonably homogeneous horizontally, the x- and y size is expected to have a small influence while the increased height should allow for more cloud formation. Initial values are taken from the ERA5 re-analysis, and this dataset is also used for the subsidence, advection and nudging terms. Using a spin-up time of 1 hour, 6 months in 2019 (Jan, Feb, Mar, Jun, Jul, Aug) are simulated daily using an uncoupled model and a coupled model and several soil settings. For location Cabauw the simulation settings are:

- Average soil, uncoupled
- Average soil, coupled
- Medium-fine soil, coupled
- Cabauw soil, coupled

These are chosen both to compare the uncoupled and coupled model for the standard soil, and to compare the soil type used by ERA5 (medium-fine soil) and the parameters from soil measurements (Cabauw soil).

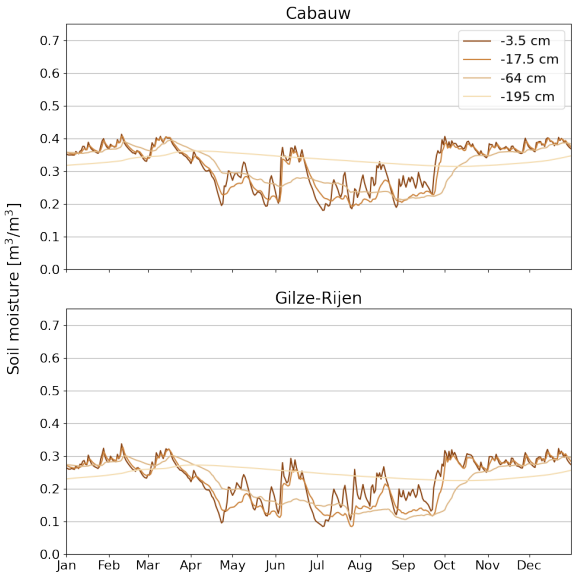

Figure 5.2: *Time series of soil moisture in 2019 from the ERA5 re-analysis in Cabauw and Gilze-Rijen, used as initial condition.*

For Gilze-Rijen, the average soil is compared to the soil used by ERA5:

- Average soil, coupled
- Coarse soil, coupled

In section 4 it was shown that the initial conditions are of vital importance to results, combined with the permanent wilting point and field capacity of the used soil type. Therefore, from figure 4.2 and the timeseries of soil moisture from ERA5 (used as initial condition), shown in figure 5.2 several hypotheses can be drawn. In both locations the soil moisture is reasonably constant in winter and drops in a short amount of time ± 1.5 m^3/m^3 to the summer values. Because of these two soil moisture regimes, the summer months and winter months are considered separately.

- In Cabauw in winter, the soil moisture is between 0.35 and 0.4 m^3/m^3, which is above the field capacities of the average soil and medium-fine soil. Therefore no large difference is expected between those settings. The 'Cabauw' settings are expected to have less evaporation and therefore a warmer and drier atmosphere.
- In Cabauw in summer, the soil moisture is frequently under the permanent wilting point of the 'Cabauw' settings. The medium-fine soil setting should have more evaporation than average soil setting and therefore should cause a slightly colder and more humid atmosphere.
- In Gilze-Rijen in winter, soil moisture is between 0.2 and 0.3 m^3/m^3, which is above field capacity for the coarse soil setting and in the regime between wilting point and field capacity point for the average soil setting.
- In Gilze-Rijen in summer, there is a large variation in soil moisture but soil moisture values are usually below 0.2 m^3/m^3. This is close to the permanent wilting point of the average soil so many days with very little evaporation are expected, resulting in high temperatures and low humidity. In the coarse settings the soil moisture is usually in the regime between permanent wilting point and field capacity point, and better model skills are expected for that reason.

5.2 Results

The variables that are compared with observations and between model settings will be temperature, humidity and wind speed in the atmosphere. To illustrate the output used in this section, the daily mean 2 m temperature in Cabauw from the average soil, uncoupled simulations is shown in figure 5.3. The main observation in this figure is the higher variance in the GRASP simulations than in the ERA5 reanalysis dataset. The statistics of the model output for the settings described above is further explored in this section, starting with a comparison between two domain sizes. The absolute values of the statistics including the error margins can be found in the appendix in tables A1-A3.

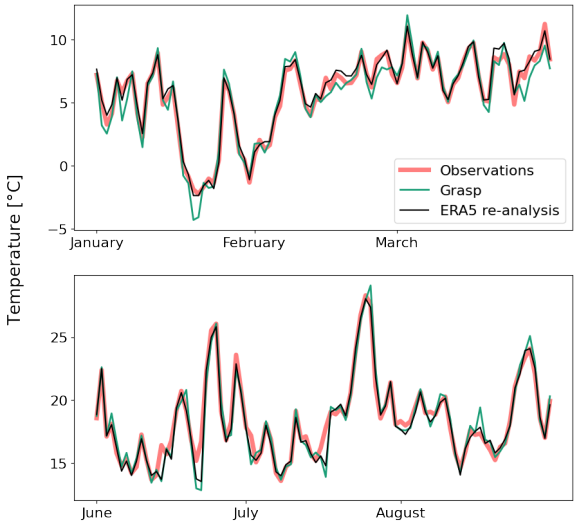

Figure 5.3: *Daily mean temperature at 2 m over the full simulation period, using the average soil setting without coupling. Observations and ERA5 re-analysis are plotted for comparison.*

5.2.1 Domain size

The difference between a small and large domain is shown for the most basic case: an uncoupled system with average soil. The percentual biases (with respected to observations) are shown in figure 5.4, separated per season and atmospheric condition. The rain biases for both seasons combined are shown in table 5.1. The cloudy days are determined using the observation of shortwave radiation reaching the surface. According to Matuszko [2012], clouds block between 40% and 85% of shortwave radiation. In this study, the fraction of shortwave radiation reaching surface compared to potential clear sky radiation $\frac{SWD_{obs}}{SWD_{clear}}$

is used to divide the data by half into cloudy days and not cloudy days. A scatter plot of the effect of the shortwave radiation bias on temperature is shown in figure 5.5.

These results show a strong underestimation of precipitation and an overestimation of shortwave radiation. There are not enough clouds formed in the simulation and there is more energy and less water reaching the surface than in reality. This surplus of energy will affect the atmosphere through surface latent and sensible heating, but the lack of clouds and rain will also cause a warmer and drier atmosphere because moist and cold air is not brought down from higher atmospheric levels to the surface by the precipitation. There will therefore be an extra positive bias in temperature and an extra negative bias in humidity added to the one present in dry conditions. If the bias on clear days is of the opposite sign to the additional cloudy bias, these could actually and give the impression that the model behaves better during cloudy days. This is especially visible in winter temperatures. Simply speaking, the modelled atmosphere has the same temperature on dry and rainy days. On clear days this is about 0.4° colder than the observations but since on cloudy days the observed atmosphere is colder, the negative temperature bias on dry days disappears. The same mechanism is present in summer, but since the modelled temperature is close to observations on clear days, on rainy days the additional bias results in an overestimation in temperature.

As expected, the big domain allows for more cloud formation, reflecting more of the incoming solar radiation and producing some rain. There is still too little precipitation and too much shortwave radiation reaching the surface in summer. In the sections below, the big domain is used in comparisons, so the remaining biases for cloudy conditions should be taken into consideration when comparing the coupling and soil settings.

5.2.2 The influence of coupling

The comparison between the uncoupled system and a coupled system in which rain is allowed to enter the soil is made here, using the big domain described above. The biases with respect to observations are shown in figure 5.4, which holds the answer the the first part of the second research question.

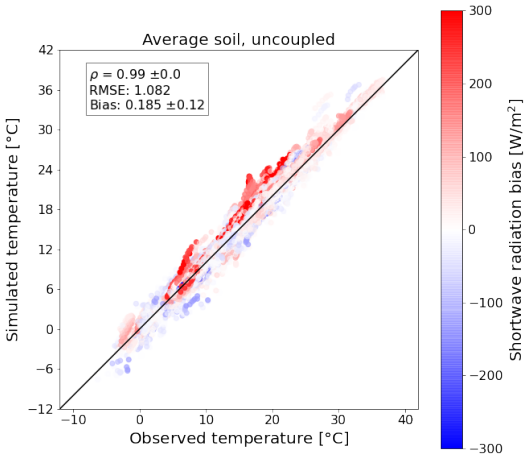

Figure 5.5: *Scatter plot of simulated and observed temperature at Cabauw using the average soil setting with the bias in shortwave down radiation as marker colors.*

The effect of coupling is expected to increase latent heating through the extra soil moisture, and this is indeed visible in the biases. When looking at the total bias this is almost entire eliminated in both seasons, through a general increase in latent heat flux. In winter, this bias reduces almost by half for the coupled system on cloudy days, while on the clear days the overestimation is also increased. Since the soil moisture is above the field capacity point in winter, extra soil moisture was not expected to influence the amount of latent heating from the soil. This large bias reduction points to a strong increase in evaporation from the interception reservoir, showing the importance of direct evaporation before the water enters the soil. The decrease of sensible heating (as a result of the Bowen ratio) decreases the temperature and increases humidity, coming closer to observations except for the winter temperature since this was already underestimated. So apart from it being more physical (in the uncoupled situation rain disappears), this figure shows a positive effect on the model skill of the rain-soil moisture coupling.

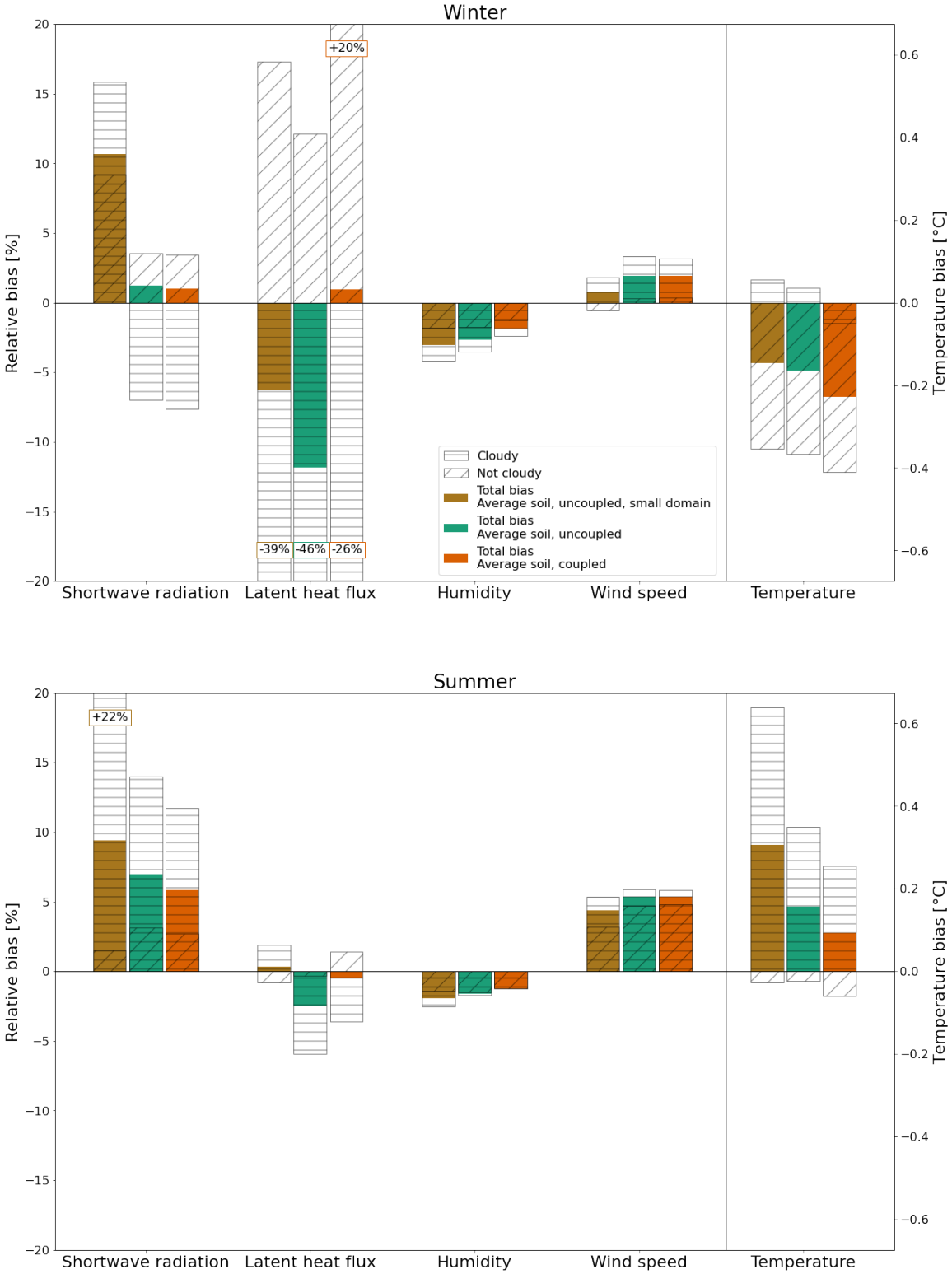

Figure 5.4: *Bar plot showing percentual biases in shortwave radiation, latent heat flux, humidity and wind speed and the absolute bias in temperature, separated into seasons and for several model settings. The simulated days are also separated by cloudiness, where the horizontal stripes show the bias during the most cloudy days and the slanted stripes show the bias during the least cloudy days.*

Location	Cabauw					Gilze-Rijen	
Soil type	Average	Average	Average	Medium-fine	Cabauw	Average	Coarse
Coupling	Uncoupled	Uncoupled	Coupled	Coupled	Coupled	Coupled	Coupled
Domain	Small	Big	Big	Big	Big	Big	Big
Rain bias	-99 %	-74 %	-72 %	-73 %	-74 %	-71 %	-73 %

Table 5.1: *Percentual biases of rain for both locations and all simulations settings, using all days in the 6 months of data*

5.2.3 Soil type differentiation

The second part of the second research question is answered in this section by comparing statistics of model skill for the simulations with different soil types.

The statistical results are plotted in Taylor diagrams in figure 5.10 for Gilze-Rijen and figure 5.11 for Cabauw, separated in summer and winter. The stars in these diagrams represent the observations. The radial distance from the origin (x,y-axes) shows the standard deviation, which is normalized to allow plotting variables with different units in a single diagram. The distance from the star shows the RMSE between model and observations and the angle with the x-axis shows the correlation. See Taylor [2001] for the theoretical basis behind this plot.

In figure 5.10 there is a small increase in skill in winter for the coarse soil, while summer shows a clear increased skill for the site-specific soil setting in all statistics and for all variables, as the markers move closer the dashed line. Figure 5.11 shows the same pattern, with small differences in winter and larger improvements in skill in summer. ERA5, which is used to initialize still outperforms GRASP in temperature and humidity, in wind speed GRASP has a higher correlation, lower RMSE and closer standard deviation. In general, the ERA5 re-analysis markers have low standard devation, which is an effect of the smoothing that is done to that dataset. Smoothing brings the standard deviation down, but in general does improve correlation.

The setting labelled 'Cabauw' soil has parameters from soil measurements, but performs poorly in all conditions and seasons. This confirms that not the absolute values, but the relation between the soil parameters and initial conditions is important to get realistic results. While the parameters are probably more accurate than the medium-fine or average setting, when using initial conditions from ERA5 reanalysis the settings that produced those conditions will give the most accurate surface fluxes and best results in the atmosphere as well. This effect will be less extreme if a longer simulation would be performed. Since these simulations were run in single days, The system did not have time to adjust, when in time the soil moisture would have reached values that are in the regime of the 'Cabauw soil' settings. Also, in figure 3.2 it was shown that the ERA5 dataset underestimates the actual soil moisture and that the ERA5-land product is closer to observations. That dataset or the observational data matches much better the 'Cabauw' soil parameters. Using those more accurate soil moisture values as initial conditions would probably produce more realistic results and might provide better skills even than the ERA5 data combined with the medium-fine soil as these are the more realistic values. The use of observations for initialization was not extensively tested in this research though, so further research is necessary to confirm this.

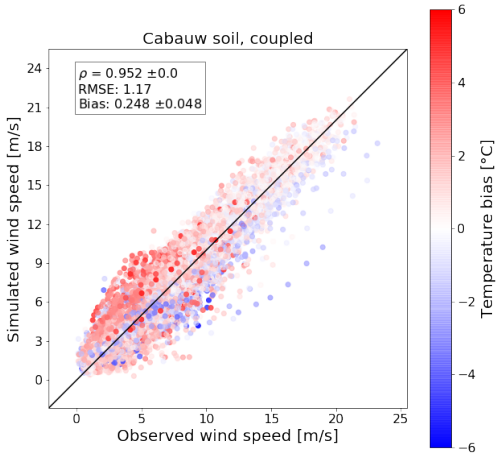

Figure 5.6: *Scatter plot of simulated and observed wind speed at Cabauw using the Cabauw soil parameters with bias in temperature as marker colors.*

The percentual biases of the different soil type simulation are shown in figures 5.7 and 5.12. Using the site specific soil types (medium-fine for Cabauw and coarse for Gilze-Rijen), the general trend is a drop in temperature and a rise in humidity, which was expected from the stress function curves. In summer this effect is more pronounced because the soil is drier. In Gilze-Rijen, the coarse soil strongly reduces the positive temperature bias in summer to a negative bias, while in winter the negative bias becomes larger. The wind speeds also decrease slightly for the coarse soil. In Cabauw similar but smaller differences are visible, improving the skills by a decrease in temperature and increase in humidity, but with no significant changes in wind speed bias. The biases confirm that the 'Cabauw' soil does not produce realistic results, with high temperatures and low humidity's that are a result of low latent heating.

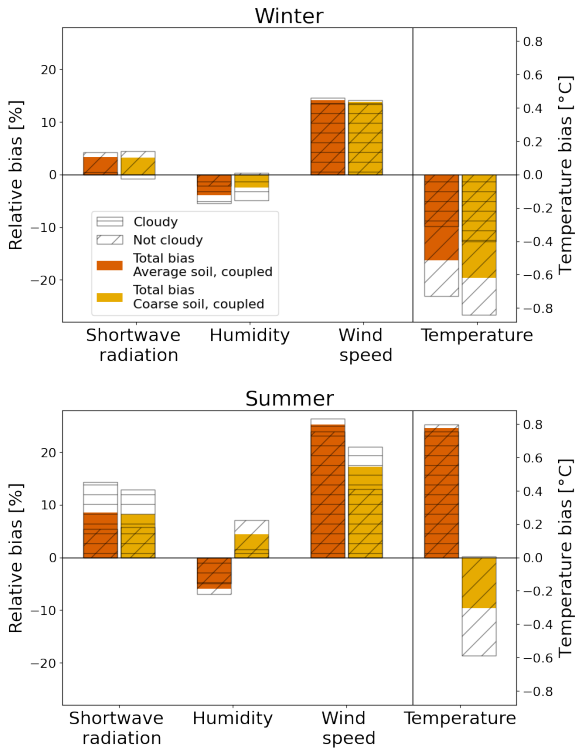

Figure 5.7: *Bar plot showing percentual biases in shortwave radiation, humidity and wind speed and the absolute bias in temperature, separated into seasons and for several model settings. The simulated days are also separated by cloudiness, where the horizontal stripes show the bias during the most cloudy days and the slanted stripes show the bias during the least cloudy days.*

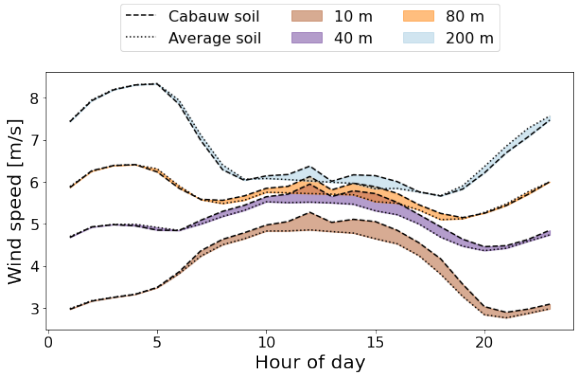

Figure 5.8: *Hourly wind speed at several heights, averaged over summer, for the Cabauw soil setting and average soil setting.*

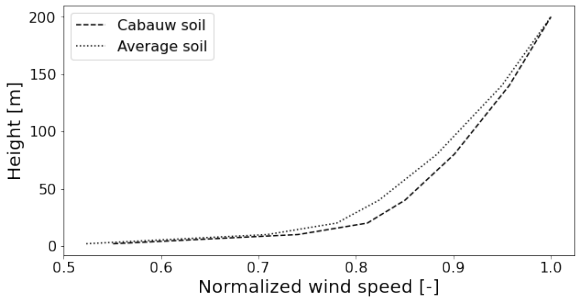

Figure 5.9: *Wind speed profiles averaged over summer days, for the Cabauw soil setting and average soil setting.*

This setting also produces higher wind speeds than the other two. A scatter plot of the simulated and observed wind speed is shown in figure 5.6, where the color of the markers indicated the bias in temperature. This figure shows a connection between temperature bias and wind speed bias. This connection could be explained using Monin-Obhukov theory [Garratt, 1995]. The increased instability by the extra heating in the 'Cabauw' soil run causes an increase in mixing in the boundary layer, mainly close to the surface. This moves the velocity vertical profile away from the logarithmic profile found in neutral conditions, resulting in increased wind speeds close to the surface and small differences at higher levels. Figure 5.8 shows the average summer wind speed at several heights for the Cabauw soil and average soil and in figure 5.9 the average profiles are shown, normalized by the 200 m wind speed. These figure confirm the larger wind speed difference close to the surface than at 200 m and clearly show the change in profile shape caused by increased mixing.

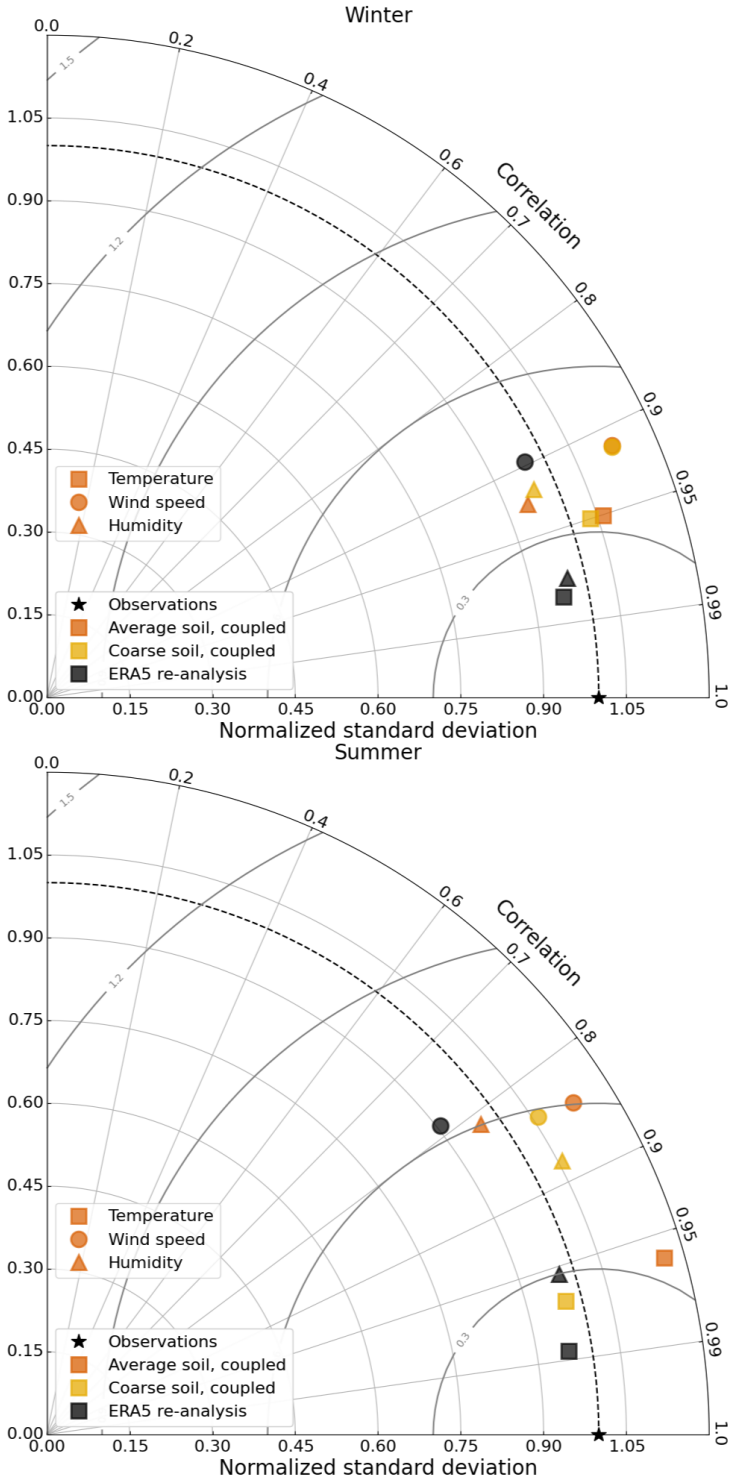

Figure 5.10: *Taylor plots showing the statistics of temperature, humidity and wind speed compared with observations in Gilze-Rijen for the ERA5 re-analysis and GRASP runs using the average soil setting and coarse soil setting.*

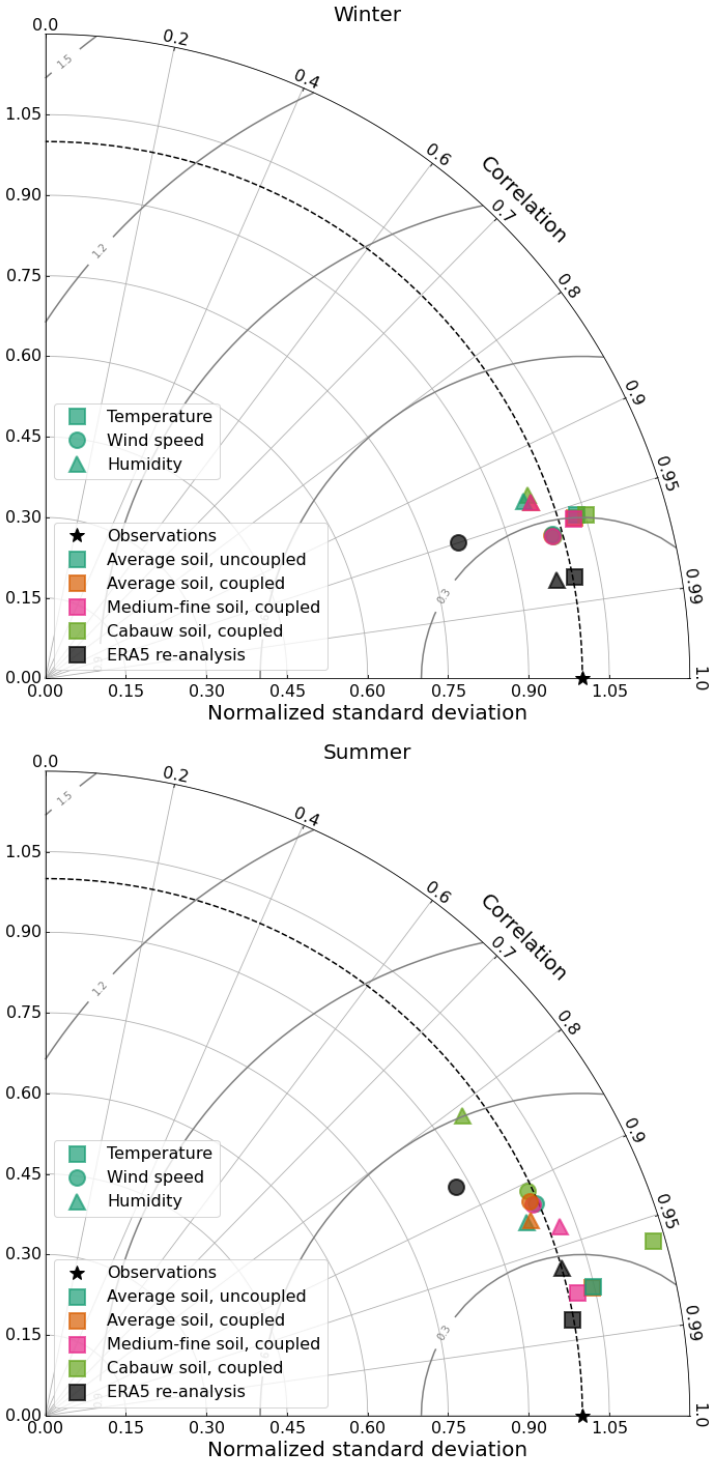

Figure 5.11: *Taylor plots showing the statistics of temperature, humidity and wind speed compared with observations in Cabauw for the ERA5 re-analysis and GRASP runs in various soil settings.*

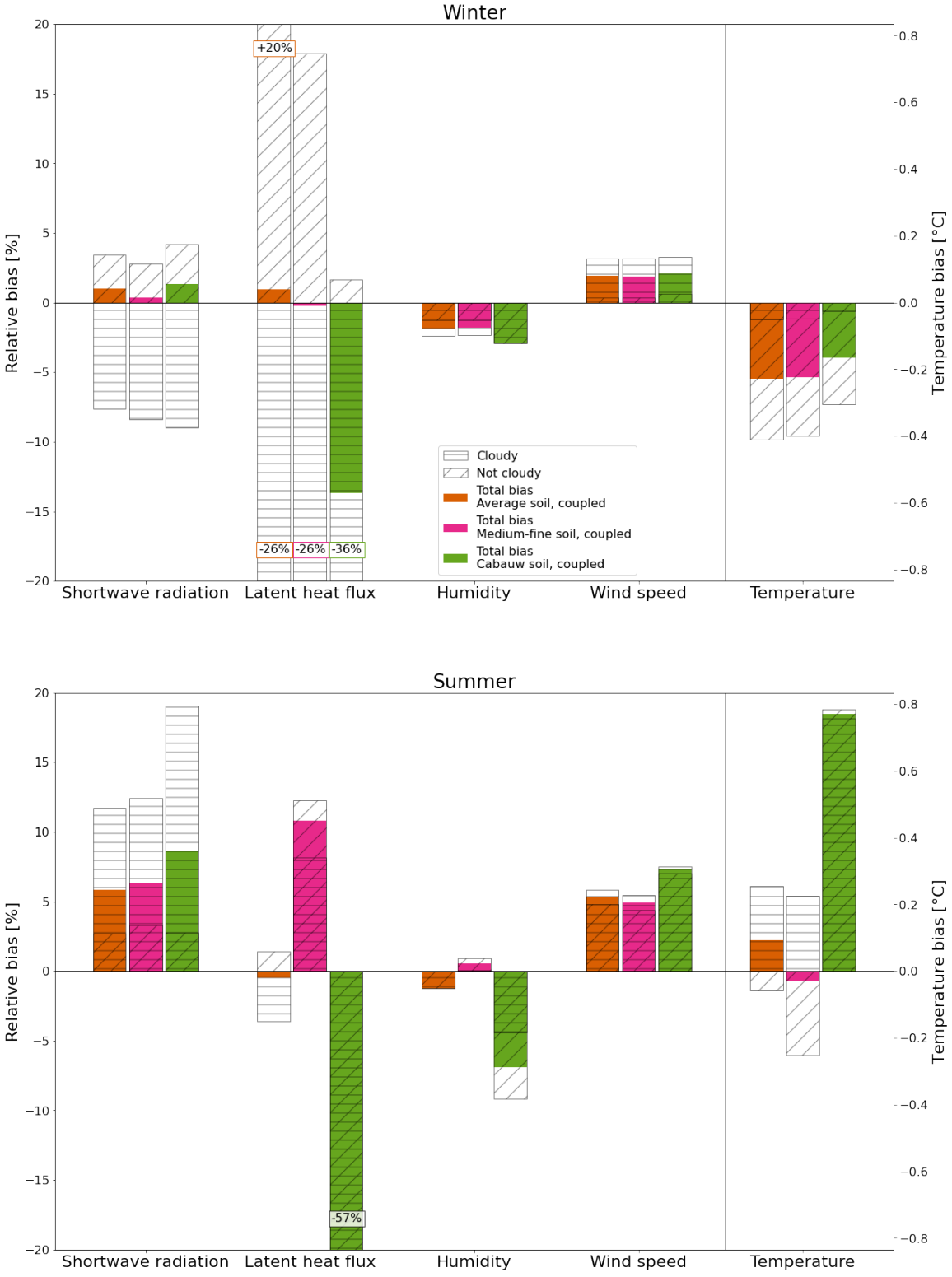

Figure 5.12: *Bar plot showing percentual biases in shortwave radiation, latent heat flux, humidity and wind speed and the absolute bias in temperature, separated into seasons and for several model settings. The simulated days are also separated by cloudiness, where the horizontal stripes show the bias during the most cloudy days and the slanted stripes show the bias during the least cloudy days.*

6 Radiation Fog

Radiation fog occurs when the surface cools after sunset by emitting longwave radiation. When the near-surface air temperature drops beneath the dewpoint temperature, water condenses thereby creating fog. This fog layer will grow during the night, reaching depths of several hundred meters. When the sun comes up in the morning, the soil warms and lifts the fog at the surface, after which it will dissipate from the ground up. In this section the reproduction of radiation fog by GRASP is studied, aimed to answer the third research question. Firstly the dataset generated in the previous section is used and secondly a case study is performed.

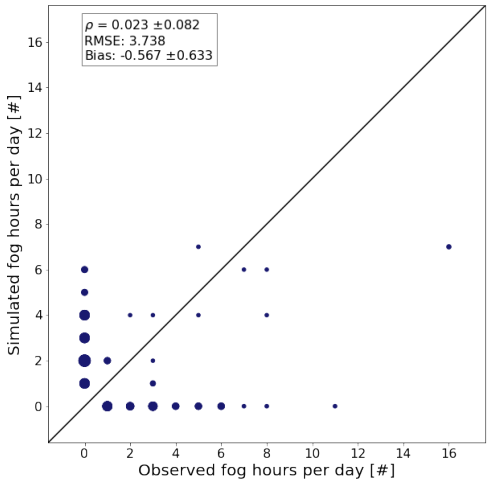

Figure 6.1: *Scatter plot showing the number of hours per day in which fog was observed and/or simulated. The size of the markers shows the number of days.*

6.1 Radiation fog reproduction in 2019 runs

As the medium-fine soil performs best at Cabauw when looking at the general statistics, this setting is used here to examine the reproduction of radiation fog close the the ground. Figure 6.1 shows the number of hours in per day that there was fog present close to the ground, with the medium-fine simulation on the y-axis and observations on the x-axis. This graph only includes the days with fog in either simulation or observation, so the days with agreement on the absence of fog are left out. In the observations there were 41 with fog present, mostly in winter. In 23 out of those 42 days with fog there was also fog in the simulations at 16m. There were an additional 43 days when there was fog in the simulation but not in the observations. Furthermore, it seems that when fog occurs in both simulation and observation, the amount of hours has reasonable agreement with observations. Everything combined, there is an negative bias of approximately half an hour of fog in the simulations. This underestimation could be down to a number of factors, and to investigate this further a case study is performed below.

6.2 Case study

The case study described by Maronga and Bosveld [2017] is replicated here: the night of 22-23 March 2011 at Cabauw. This case was also replicated by Van Tiggelen et al. [2018] using the LES model DALES. 4 key moments in the lifetime of a fog layer are described by Maronga and Bosveld [2017]:

- Formation: The time when q_l reaches 0.01 g/kg for the first time anywhere near the surface.
- Maximum: The time of the maximum q_l anywhere in the fog layer.
- Lifting: The time when the q_l drops beneath 0.01 g/kg in the lowest atmospheric level for the first time since formation.
- Dissipation: The time when q_l is below 0.01 g/kg in all levels in the bottom 400m of the atmosphere.

During the night of 23 March, a deep fog layer developed with formation before midnight, sunrise around 5:45 in the morning dissipation around 9:00. A detailed description of the case can be found in Boers et al. [2013].

6.3 Set-up

According to Maronga and Bosveld [2017], a fine resolution is necessary to accurately resolve the turbulence that is necessary to mix the cold air from the surface vertically so that a fog layer can form and to ensure a sharp inversion layer. Two domains are used here, the lower resolution domain being 1280 m x 1280 m x 1000 m with a resolution of 10 m in x and

y direction and a stretched vertical resolution starting at 3 m at the surface. The high resolution domain is smaller, namely 128 m x 128 m x 1000 m with a resolution of 2 m in x and y direction and a stretched vertical resolution in z direction starting at 1 m at the surface. All cases are run with the medium-fine soil and coupled system.

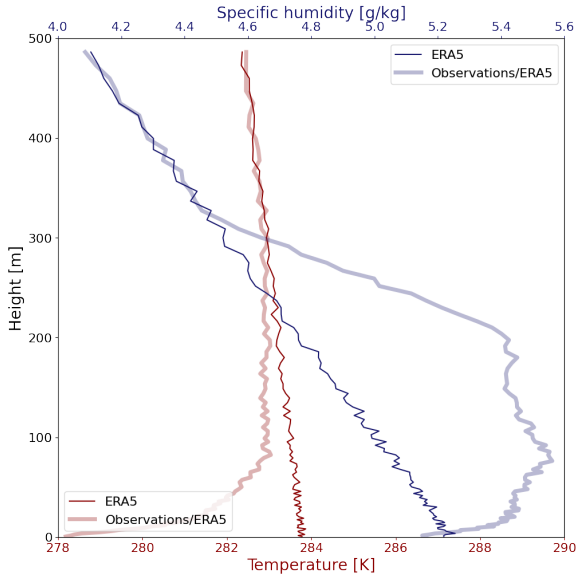

Figure 6.2: *Initial profiles of temperature and specific humidity at 22:00 used in the ERA5 runs (thin line) and in the observation initialized runs (thick line).*

The case labelled ERA5 is done in the same way as the runs in section 5, using ERA5 re-analysis data as input for all variables and nudging to the ERA5 data during the run. All runs shown here are initialized at 22:00 on 22 March, with the first 2 hours used as spin-up time. In the second run, labelled 'Obs initialized', the bottom 200m of the atmosphere set by the observations at 22:00, while the layers above are still set by ERA5. This simulation is only nudged to ERA5 data at the top of the domain. The third run ('Obs initialized and nudged') has similar set-up, except that this run is nudged at the surface to the observed profiles from the measurement tower. The initial temperature and specific humidity profiles up to 500 m for these runs are shown in figure 6.2, showing that the ERA5 re-analysis has a higher temperature and lower specific humidity than the observed profiles.

Maronga and Bosveld [2017] showed that the soil moisture influences the dissipation of the fog layer through the Bowen ratio (sensible/latent heating). A high soil moisture lowers the Bowen ratio, causing a longer fog lifetime, while a dry soil heats the atmosphere quicker, dissipating the fog and reducing its lifetime. This is tested in the fourth run ('Obs initialized, dry soil'), which has the same set-up as the 'Obs initialized' case but has a lowered soil moisture that falls below the field capacity of the medium soil, namely 0.25 m^3/m^3 for all soil layers.

6.4 Results

The relative humidity contours for all runs are plotted in figure 6.3, along with the observations from the Cabauw measurement tower. The solid line is the 99% relative humidity contour, the dashed lines are liquid water content contours at 0.1 g/kg intervals. The circle, cross and square are plotted at the maximum, lifting and dissipation times, respectively. The exact time markers can be found in table 6.1. Contour plots of the liquid water content can be found in the appendix in figure A1 for comparison to the figures in Maronga and Bosveld [2017]. For all simulation except the low resolution case, fog developed during the spin-up time (before 00:00 UTC). Further comparing the low and high resolution cases, we can see a shallower fog layer in the low resolution case reaching to 50 m and dissipation quickly after lifting, almost an hour sooner than the high resolution case. In the middle two graphs of figure 6.3 we can see that initialization with observations leads to a much deeper and denser fog layer than initializing with ERA5 data. Since figure 6.2 showed that ERA5 underestimated the humidity in the evening, this was to be expected. However, the degree of dependence on the initial atmosphere of the development of the fog layer is promising, as that means observations at one moment in the evening can strongly improve the simulation of fog. The 'Obs initialized and nudged' contour plot, which should be the most realistic, shows a similar fog layer in depth and density, but the dissipation happens approximately 1 hour quicker than the run that was not nudged. The run with dry soil looks very similar to the 'Obs initialized' run, but a small difference can be seen in the dissipation time, which is 15 minutes earlier.

The atmospheric profiles at various times of night are plotted in figure 6.4. In these profiles the initialized and nudged run is closest to observations as expected. During the night the simulations show a much sharper inversion than the observations and the near-surface temperature and humidity are lower than observed. At 06:00, the height of the inversion is reasonably accurate for the runs that used observa-

tions, while the ERA5 run clearly has a too shallow fog layer at this moment. At 10:00 there is no inversion visible anymore in the observations or the ERA5 run, showing the fog is completely dissipated in the bottom 200 m of the atmosphere. The observations initialized run shows a sharper inversion around 200 m than the initialized and nudged run, which agrees with the faster dissipation of the nudged run. In general these figures show that the depth of the fog layer is well replicated when using observational profiles for initialization, but the intensity of the fog layer and its capping are stronger than in observations, causing the dissipation to take longer. Some reasons for this are the relatively small domain and periodic boundary conditions combined with the absence of nudging at the surface, resulting in the absence of larger-scale processes influencing the atmosphere near the surface. Also, an underestimation of turbulent mixing can cause the strong inversion and increase the time necessary for full dissipation.

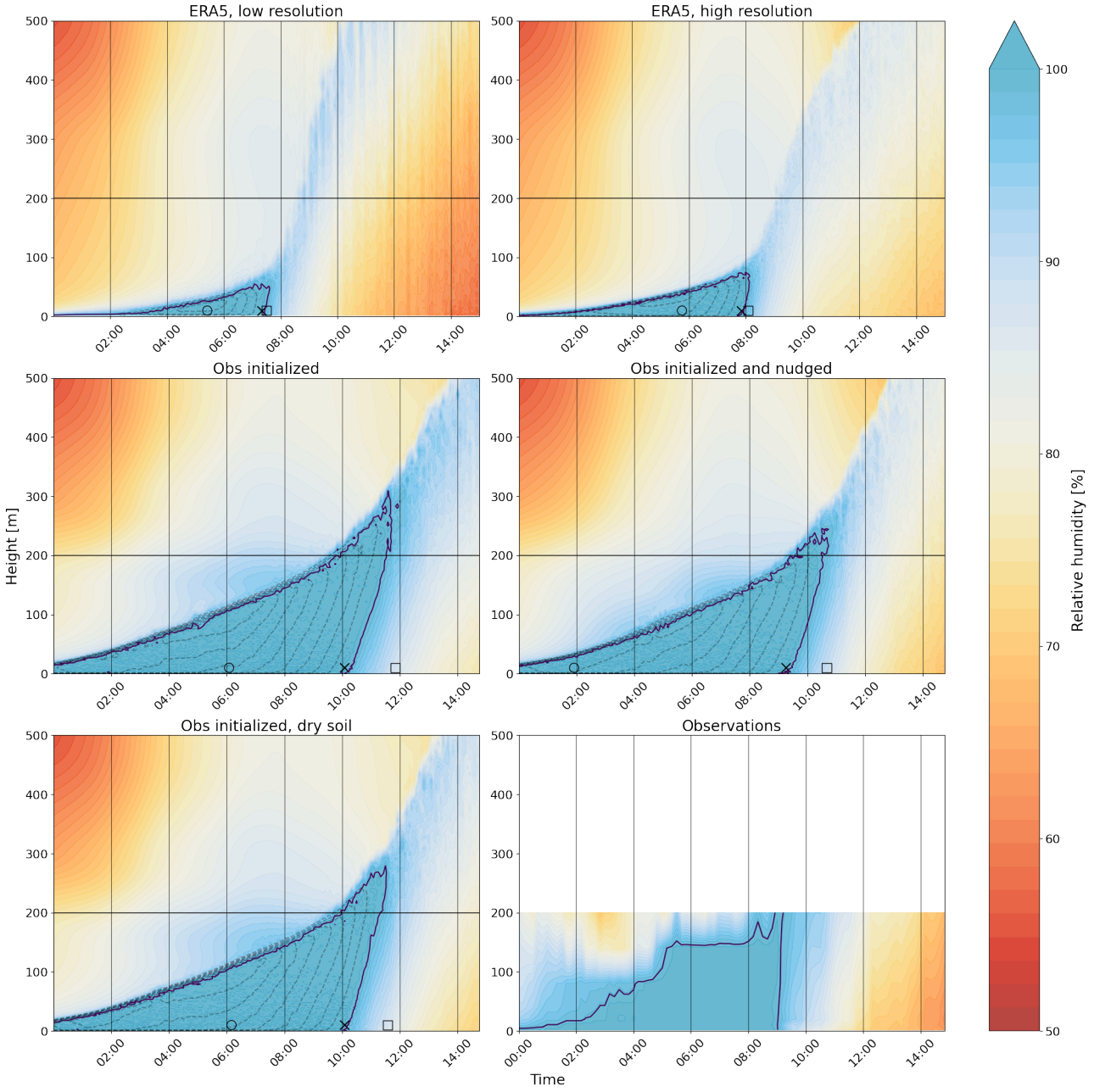

Figure 6.3: *Contour plots of relative humidity for the night of 22-23 March 2011. The solid line is the 99% relative humidity contour, the dashed lines are liquid water content contours at 0.1 g/kg intervals. The circles, crosses and squares are the maximum, lifting and dissipation times, respectively.*

Time (UTC)	Formation	Maximum	Lifting	Dissipation
ERA5, low resolution 10 m x 10 m x 3 m at surface	00:40	05:25	07:20	07:30
ERA5, high resolution 2 m x 2 m x 1 m at surface	<00:00	05:20	08:10	08:35
Obs initialized No nudging at surface	<00:00	06:05	10:05	11:50
Obs initialized and nudged Surface nudging to observations	<00:00	01:55	09:15	10:40
Obs initialized, dry soil $q_s = 0.25$ m^3/m^3	<00:00	06:10	10:05	11:35

Table 6.1: *Moments during the simulation of fog formation, maximum, lifting and dissipation in all runs.*

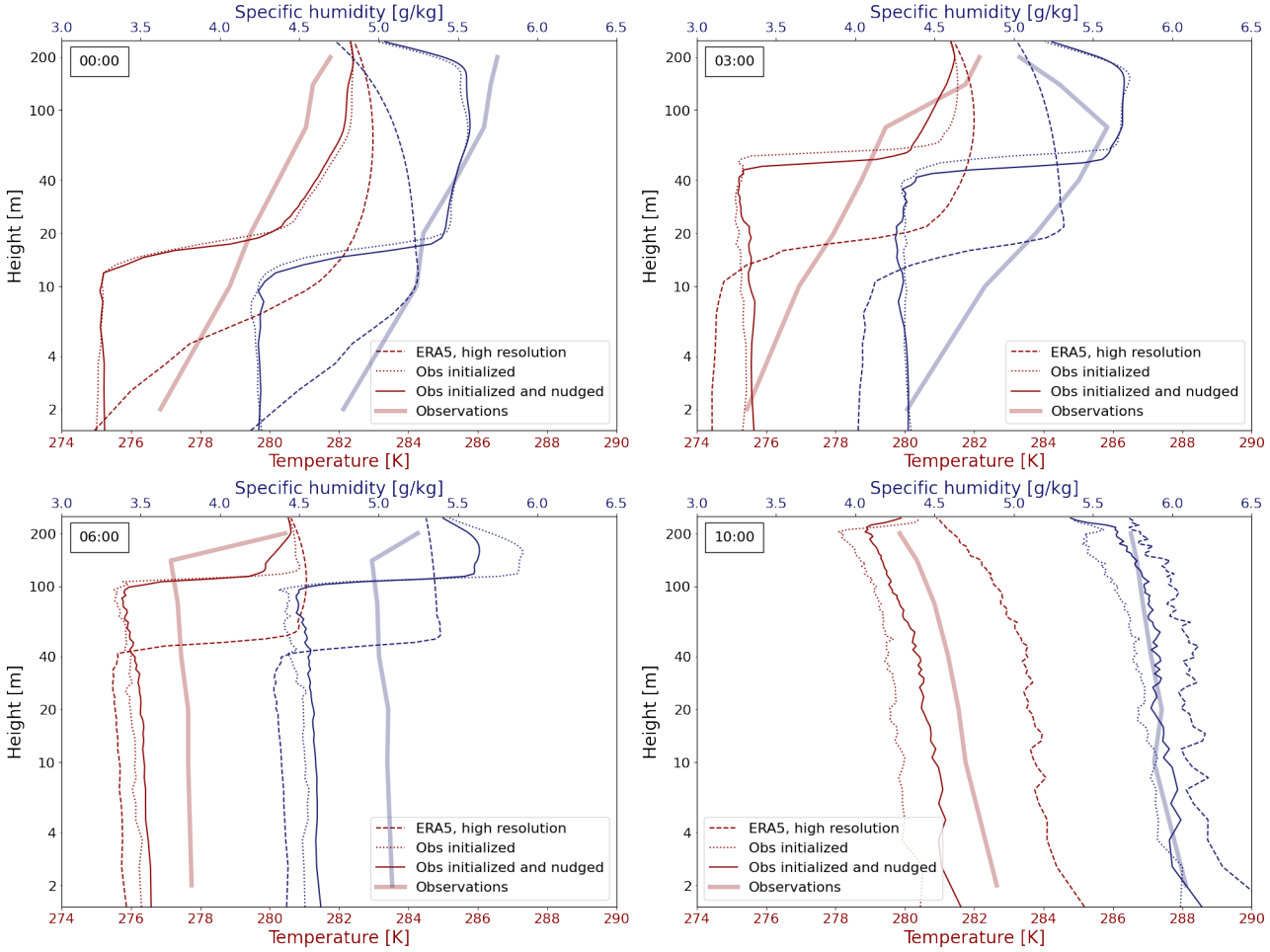

Figure 6.4: *Atmospheric profiles of temperature and specific humidity for 3 runs and observations on a vertical logarithmic scale at several times of night and morning.*

7 Conclusions

The first part of this study was aimed to understand the coupled TESSEL-LES system and find the sensitivities of soil parameters and initial conditions to soil moisture, thereby answering the first research question. The sensitivity tests showed the importance of matching the soil parameters to the initial soil moisture, especially when running simulations of one day. A mismatch between these two factors can cause extremely high Bowen ratio's which strongly influence the atmosphere within 24 hours.

The second research question asked whether rain-soil moisture coupling and soil type differentiation would improve modellings skills. This question was answered using 6 months of daily runs, specifically January-March and June-August in 2019. In these runs a comparison between domain sizes showed that a higher domain allows for more convection, leading to increased cloud formation and rain. The larger domain was therefore used to compare an uncoupled and coupled system. Between these two set-ups there was no significant difference in Taylor plots showing correlation, RMSE and standard deviation. A large difference was visible in the variable biases, where the coupled system showed a smaller latent heat flux, summer temperature and humidity bias, mainly in cloudy conditions. The second comparison was made between the average soil type which is the default input in GRASP and the site-specific soil types in Cabauw and Gilze-Rijen, as well as a soil type extra-specific for the Cabauw site. Between these set-ups there was a difference visible in the summer Taylor plots, where the site-specific soil type showed an improved skill in terms of correlation and RMSE. When looking at the biases, a similar result was found, with decreased biases in humidity, temperature and wind speed, even though the latent heat flux bias increased. The extra-specific 'Cabauw' soil showed a strong decrease in skill, with a negative bias of 57% in latent heat flux causing a negative bias in humidity and positive bias in temperature. This also resulted in an increased wind speed bias, which could be explained by a larger deviation from the logarithmic wind profile as a result of larger instability, following the Monin-Obhukov theory. From these results it can be concluded that soil type has a large influence on the near-surface atmosphere in LES runs that were initialized and nudged by a large-scale dataset (ERA5). Using the soil type provided by ECMWF increased model skill, especially in summer. The extra specific soil parameters derived from observations resulted in a poor model performance, showing that it is more beneficiary to match the parameters to the initial conditions rather than using the most realistic ones.

In the Cabauw runs the reproduction of radiation fog was also studied and the predictability of fog in this set-up was found to be quite poor, with the amount of fog hours per day having almost no correlation with observations. A case study was therefore performed to find sensitivities in predicting radiation fog. The night of 22-23 March 2011 was run in different set-ups varying resolution, initialization, nudging and initial soil moisture. From the height of the fog layer and the key points of time, it was concluded that a high resolution is key to producing accurate fog layers in simulations, and that initialization with observational profiles at 22:00 strongly improved the fog layer depth during the night. The times of lifting and dissipation were later than observed, halving the initial soil moisture quickened this by 15 minutes. These conclusions are all in agreement with Maronga and Bosveld [2017], where the same case was studied.

8 Recommendations & Outlook

Model capabilities

Although the version of TESSEL used in this research is complex and takes into account many soil processes, some possible improvements are described here.

Over the years TESSEL has been continuously enhanced by ECMWF, which resulted in H-TESSEL, a hydrological enhancement of TESSEL. This new version accomodates various locations and conditions, which are discussed in detail in section 2.2. In high soil moisture conditions, the switch in the hydraulic conductivity from the Clapp-Hornberger to the van Genuchten formulation is the most prominent, which mostly influences the water transport between soil layers near the saturation moisture levels. Another adjustment was done to improve skills in dry conditions, namely the adjustment of bare soil evaporation which allows for soil moisture values below the permanent wilting point. The version of TESSEL used here has no snow tile option as of yet, while H-TESSEl has an extensive section that takes into account melting, snow aging, the insulating effect of snow and its albedo effects. In this research snowfall did not play a part, but in different regions of the world the addition of these tiles is unavoidable and should be subject to future research.

When discussing possible improvements, the ground heat flux should be addressed too, being the subject of ongoing debate in literature [Florides and Kalogirou, 2007] [Li and Lai, 2015]. While TESSEL extensively models the water interactions between land and atmosphere, the ground heat flux depends on a single empirical parameter, even though this flux plays an important part in the surface energy balance. Purdy et al. [2016] compare 6 ground heat flux model approaches, and future research could compare these in an LES set-up.

Periodic boundary conditions were used throughout this thesis. Since the domains were reasonably homogeneous it is not expected to have had a large negative influence. When heterogeneous domains are studied however, like mountains, coastal areas or areas with large obstacles, open boundary conditions should be considered. This would not only solve the re-entry of turbulence at the sides of the domain, but could also possibly include meso-scale phenomena to the large-scale forcing.

Lastly, surface runoff plays a crucial role during heavy rainfall according to ECMWF [2020], varying between 1% to 50% of the rain falling on the surface, but is not included in GRASP at this moment. During this research, it became clear that the microphysics in GRASP do not produce sufficient clouds and precipitation in this domain size. It was therefore not possible to study the behaviour of this coupled system during heavy rainfall. In this research it was shown that the rain-soil moisture coupling improves the modelling skill in relatively dry conditions, but what effect this has when excessive amounts of water reach the surface is not yet clear. Since runoff is not included in this version of TESSEL, all water will infiltrate the soil and it is expected that this will cause an excess of soil moisture. It is therefore recommended to include this in future work.

Next steps

Model improvements can be made indefinitely, adding more and more complexity and thereby more accurately grasping reality. From this study it became clear that data is paramount in predicting the division between latent and sensible heating accurately. Therefore the most headway at this point, can be achieved by obtaining accurate data of soil moisture.

First of all, an accurate map of soil classification is necessary. The dataset used by ECMwF is the FAO/UNESCO Digital Soil Map of the World (DSMW) [FAO, 2003], which is available at 10 km resolution and classifies soil into the soil types shown in table 4.1. This classification provides the model parameters that determine the range of soil moisture values found at a certain location and is therefore constant in time apart from any major geographical changes. Improving this dataset would therefore be beneficial for a long time to come.

The second part is determining soil moisture values at short time-scales, as precipitation can change the soil moisture in the course of a day. Remote sensing seems a perfect solution to get consistent data for this purpose, but the limited depth and resolution remain a problem. The efforts described in the introduction, using machine learning and combining different datasets seems promising. As in-situ measurements of soil moisture are notoriously unreliable and prone to high variability, deducing soil moisture data from other more reliable sources would be a solution that can be consistent and practical on a global scale.

References

Constantin Ardilouze, L Batté, Felix Bunzel, D Decremer, M Déqué, Francisco J Doblas-Reyes, H Douville, D Fereday, Virginie Guemas, C MacLachlan, et al. Multi-model assessment of the impact of soil moisture initialization on mid-latitude summer predictability. *Climate Dynamics*, 49(11):3959–3974, 2017.

G Balsamo, S Boussetta, E Dutra, A Beljaars, P Viterbo, and B Van den Hurk. Evolution of land surface processes in the ifs. *ECMWF newsletter*, 127(17-22):78, 2011.

Gianpaolo Balsamo, Anton Beljaars, Klaus Scipal, Pedro Viterbo, Bart van den Hurk, Martin Hirschi, and Alan K Betts. A revised hydrology for the ecmwf model: Verification from field site to terrestrial water storage and impact in the integrated forecast system. *Journal of hydrometeorology*, 10(3):623–643, 2009.

Anton CM Beljaars and Fred C Bosveld. Cabauw data for the validation of land surface parameterization schemes. *Journal of climate*, 10(6):1172–1193, 1997.

Thierry Bergot and Daniel Guedalia. Numerical forecasting of radiation fog. part i: Numerical model and sensitivity tests. *Monthly Weather Review*, 122(6):1218–1230, 1994.

R Boers, H Klein Baltink, HJ Hemink, FC Bosveld, and M Moerman. Ground-based observations and modeling of the visibility and radar reflectivity in a radiation fog layer. *Journal of Atmospheric and Oceanic Technology*, 30(2):288–300, 2013.

Steven J Böing, Harm JJ Jonker, A Pier Siebesma, and Wojciech W Grabowski. Influence of the subcloud layer on the development of a deep convective ensemble. *Journal of the Atmospheric Sciences*, 69(9):2682–2698, 2012.

Fred C Bosveld, Peter Baas, Anton Beljaars, Albert AM Holtslag, Jordi Vilà-Guerau de Arellano, and Bas JH Van De Wiel. Fifty years of atmospheric boundary-layer research at cabauw serving weather, air quality and climate. *Boundary-Layer Meteorology*, 177(2):583–612, 2020.

Souhail Boussetta, Gianpaolo Balsamo, Anton Beljaars, Tomas Kral, and Lionel Jarlan. Impact of a satellite-derived leaf area index monthly climatology in a global numerical weather prediction model. *International journal of remote sensing*, 34(9-10):3520–3542, 2013.

Mariko S Burgin, Andreas Colliander, Eni G Njoku, Steven K Chan, Francois Cabot, Yann H Kerr, Rajat Bindlish, Thomas J Jackson, Dara Entekhabi, and Simon H Yueh. A comparative study of the smap passive soil moisture product with existing satellite-based soil moisture products. *IEEE Transactions on Geoscience and Remote Sensing*, 55(5):2959–2971, 2017.

Roger B Clapp and George M Hornberger. Empirical equations for some soil hydraulic properties. *Water resources research*, 14(4):601–604, 1978.

BJ Cosby, GM Hornberger, RB Clapp, and ToR Ginn. A statistical exploration of the relationships of soil moisture characteristics to the physical properties of soils. *Water resources research*, 20(6):682–690, 1984.

Narendra N Das, Dara Entekhabi, and Eni G Njoku. An algorithm for merging smap radiometer and radar data for high-resolution soil-moisture retrieval. *IEEE Transactions on Geoscience and Remote Sensing*, 49 (5):1504–1512, 2010.

AGM Driedonks, H Van Dop, and WH Kohsiek. Meteorological observations on the 213 m mast at cabauw, in the netherlands. In *4th Symposium on Meteorological Observations and Instrumentation*, pages 41–46, 1978.

ECMWF. Ifs documentation cy47r1–part iv: Physical processes. *ECMWF, doi*, 10:150, 2020.

Bin Fang, Venkataraman Lakshmi, Rajat Bindlish, Thomas J Jackson, and Pang-Wei Liu. Evaluation and validation of a high spatial resolution satellite soil moisture product over the continental united states. *Journal of Hydrology*, 588:125043, 2020.

FAO. Digital soil map of the world (dsmw). *Technical Report, Food and Agriculture Organization of the United Nations*, 2003.

Erich M Fischer, Sonia I Seneviratne, Pier Luigi Vidale, Daniel Lüthi, and Christoph Schär. Soil moisture–atmosphere interactions during the 2003 european summer heat wave. *Journal of Climate*, 20(20):5081–5099, 2007.

Georgios Florides and Soteris Kalogirou. Ground heat exchangers—a review of systems, models and applications. *Renewable energy*, 32(15):2461–2478, 2007.

JR Garratt. *The Atmosphere Boundary Layer (Cambridge Atmospheric and Space Science Series)*, chapter 6. London: Cambridge University Press, 1995.

Manolis G Grillakis. Increase in severe and extreme soil moisture droughts for europe under climate change. *Science of The Total Environment*, 660:1245–1255, 2019.

Daniel Guedalia and Thierry Bergot. Numerical forecasting of radiation fog. part ii: A comparison of model simulation with several observed fog events. *Monthly Weather Review*, 122(6):1231–1246, 1994.

David Gustafsson, E Lewan, BJJM van den Hurk, P Viterbo, A Grelle, Anders Lindroth, E Cienciala, Meelis Mölder, Sven Halldin, and Lars-Christer Lundin. Boreal forest surface parameterization in the ecmwf model—1d test with nopex long-term data. *Journal of Applied Meteorology*, 42(1):95–112, 2003.

M Heinen, G Bakker, and JHM Wosten. Waterretentie-en doorlatendheidskarakteristieken van boven-en ondergronden in nederland: de staringreeks: Update 2018. Technical report, Wageningen Environmental Research, 2020.

Thijs Heus, Chiel C van Heerwaarden, Harmen JJ Jonker, A Pier Siebesma, S Axelsen, K Van Den Dries, O Geoffroy, AF Moene, D Pino, SR De Roode, et al. Formulation of the dutch atmospheric large-eddy simulation (dales) and overview of its applications. *Geoscientific Model Development*, 3(2):415–444, 2010.

Daniel Hillel. *Introduction to soil physics*. Academic press, 2013.

Martin Hirschi, Sonia I Seneviratne, Vesselin Alexandrov, Fredrik Boberg, Constanta Boroneant, Ole B Christensen, Herbert Formayer, Boris Orlowsky, and Petr Stepanek. Observational evidence for soil-moisture impact on hot extremes in southeastern europe. *Nature Geoscience*, 4(1):17–21, 2011.

Bruno Jacquemin and Joël Noilhan. Sensitivity study and validation of a land surface parameterization using the hapex-mobilhy data set. *Boundary-Layer Meteorology*, 52(1):93–134, 1990.

CJ Jager, TC Nakken, and CL Palland. Bodemkundig onderzoek van twee graslandpercelen nabij cabauw. *NV Heidemaatschappij Beheer*, 9, 1976.

PG Jarvis. The interpretation of the variations in leaf water potential and stomatal conductance found in canopies in the field. *Philosophical Transactions of the Royal Society of London. B, Biological Sciences*, 273 (927):593–610, 1976.

Oistein Johansen. Thermal conductivity of soils. Technical report, Cold Regions Research and Engineering Lab Hanover NH, 1977.

Randal D Koster, Paul A Dirmeyer, Zhichang Guo, Gordon Bonan, Edmond Chan, Peter Cox, CT Gordon, Shinjiro Kanae, Eva Kowalczyk, David Lawrence, et al. Regions of strong coupling between soil moisture and precipitation. *Science*, 305(5687):1138–1140, 2004a.

Randal D Koster, Max J Suarez, Ping Liu, Urszula Jambor, Aaron Berg, Michael Kistler, Rolf Reichle, Matthew Rodell, and Jay Famiglietti. Realistic initialization of land surface states: Impacts on subseasonal forecast skill. *Journal of hydrometeorology*, 5(6):1049–1063, 2004b.

Chang Suk Lee, Eunha Sohn, Jun Dong Park, and Jae-Dong Jang. Estimation of soil moisture using deep learning based on satellite data: A case study of south korea. *GIScience & Remote Sensing*, 56(1):43–67, 2019.

Min Li and Alvin CK Lai. Review of analytical models for heat transfer by vertical ground heat exchangers (ghes): A perspective of time and space scales. *Applied Energy*, 151:178–191, 2015.

B Maronga and FC Bosveld. Key parameters for the life cycle of nocturnal radiation fog: a comprehensive large-eddy simulation study. *Quarterly Journal of the Royal Meteorological Society*, 143(707):2463–2480, 2017.

Dorota Matuszko. Influence of the extent and genera of cloud cover on solar radiation intensity. *International Journal of climatology*, 32(15):2403–2414, 2012.

Binayak P Mohanty, Michael H Cosh, Venkat Lakshmi, and Carsten Montzka. Soil moisture remote sensing: State-of-the-science. *Vadose Zone Journal*, 16(1):1–9, 2017.

CD Peters-Lidard, E Blackburn, X Liang, and Eric F Wood. The effect of soil thermal conductivity parameterization on surface energy fluxes and temperatures. *Journal of the Atmospheric Sciences*, 55(7):1209–1224, 1998.

AJ Purdy, JB Fisher, ML Goulden, and JS Famiglietti. Ground heat flux: An analytical review of 6 models evaluated at 88 sites and globally. *Journal of Geophysical Research: Biogeosciences*, 121(12):3045–3059, 2016.

Jerôme Schalkwijk, Harmen JJ Jonker, A Pier Siebesma, and Erik Van Meijgaard. Weather forecasting using gpu-based large-eddy simulations. *Bulletin of the American Meteorological Society*, 96(5):715–723, 2015.

Sonia I Seneviratne, Randal D Koster, Zhichang Guo, Paul A Dirmeyer, Eva Kowalczyk, David Lawrence, Ping Liu, David Mocko, Cheng-Hsuan Lu, Keith W Oleson, et al. Soil moisture memory in agcm simulations: analysis of global land–atmosphere coupling experiment (glace) data. *Journal of Hydrometeorology*, 7(5): 1090–1112, 2006.

Sonia I Seneviratne, Thierry Corti, Edouard L Davin, Martin Hirschi, Eric B Jaeger, Irene Lehner, Boris Orlowsky, and Adriaan J Teuling. Investigating soil moisture–climate interactions in a changing climate: A review. *Earth-Science Reviews*, 99(3-4):125–161, 2010.

Susha Lekshmi SU, Devendra Narain Singh, and Maryam Shojaei Baghini. A critical review of soil moisture measurement. *Measurement*, 54:92–105, 2014.

Karl E Taylor. Summarizing multiple aspects of model performance in a single diagram. *Journal of geophysical research: atmospheres*, 106(D7):7183–7192, 2001.

Bart JJM van den Hurk, P Viterbo, ACM Beljaars, and AK Betts. *Offline validation of the ERA40 surface scheme*, volume 295. European Centre for Medium-Range Weather Forecasts Reading, UK, 2000.

M Th Van Genuchten. A closed-form equation for predicting the hydraulic conductivity of unsaturated soils. *Soil science society of America journal*, 44(5):892–898, 1980.

Maurice Van Tiggelen, SR de Roode, A Siebesma, and B van de Wiel. Towards improving the land-surface-atmosphere coupling in the dutch atmospheric large-eddy simulation model (dales). *Delft University of Technology, the Netherlands. Master's thesis. http://resolver. tudelft. nl/uuid: bbe384d1-3f40-487a-b1a6-7c e 34438f2db*, 2018.

Pedro Viterbo and Anton CM Beljaars. An improved land surface parameterization scheme in the ecmwf model and its validation. *Journal of climate*, 8(11):2716–2748, 1995.

Xubin Zeng, Yong-Jiu Dai, Robert E Dickinson, and Muhammad Shaikh. The role of root distribution for climate simulation over land. *Geophysical Research Letters*, 25(24):4533–4536, 1998.

Appendix

Season	Variable	Setting	Correlation	Bias	RMSE
Winter	Humidity [g/kg]	Average soil, coupled	0.93 ± 0.00	-0.19 ± 0.05	0.46
		Coarse soil, coupled	0.92 ± 0.00	-0.12 ± 0.05	0.46
	Shortwave radiation [W/m^2]	Average soil, coupled	0.92 ± 0.00	4.83 ± 9.92	60.48
		Coarse soil, coupled	0.93 ± 0.00	4.71 ± 9.94	58.66
	Temperature [°C]	Average soil, coupled	0.95 ± 0.00	-0.52 ± 0.19	1.52
		Coarse soil, coupled	0.95 ± 0.00	-0.62 ± 0.19	1.54
	Wind speed [m/s]	Average soil, coupled	0.91 ± 0.00	0.57 ± 0.10	1.19
		Coarse soil, coupled	0.91 ± 0.00	0.55 ± 0.10	1.17
Summer	Humidity [g/kg]	Average soil, coupled	0.81 ± 0.01	-0.56 ± 0.09	1.16
		Coarse soil, coupled	0.88 ± 0.00	0.42 ± 0.09	0.98
	Shortwave radiation [W/m^2]	Average soil, coupled	0.94 ± 0.00	27.01 ± 17.23	98.88
		Coarse soil, coupled	0.93 ± 0.00	26.44 ± 15.59	100.57
	Temperature [°C]	Average soil, coupled	0.96 ± 0.00	0.78 ± 0.31	1.99
		Coarse soil, coupled	0.97 ± 0.00	-0.30 ± 0.27	1.44
	Wind speed [m/s]	Average soil, coupled	0.85 ± 0.01	0.72 ± 0.09	1.21
		Coarse soil, coupled	0.84 ± 0.00	0.49 ± 0.08	1.04

Table A1: *Statistics from runs in Gilze-Rijen for all settings and seasons.*

Variable	Setting	Correlation	Bias	RMSE
Humidity [g/kg]	Average soil, uncoupled, small	0.94 ± 0.00	-0.14 ± 0.02	0.41
	Average soil, uncoupled	0.94 ± 0.00	-0.12 ± 0.02	0.40
	Average soil, coupled	0.94 ± 0.00	-0.09 ± 0.02	0.39
	Medium-fine soil, coupled	0.94 ± 0.00	-0.08 ± 0.02	0.39
	Cabauw soil, coupled	0.93 ± 0.00	-0.14 ± 0.02	0.42
Latent heat flux [W/m^2]	Average soil, uncoupled, small	0.83 ± 0.00	-1.52 ± 2.00	28.54
	Average soil, uncoupled	0.81 ± 0.01	-2.90 ± 1.98	30.57
	Average soil, coupled	0.84 ± 0.00	0.23 ± 1.98	28.11
	Medium-fine soil, coupled	0.84 ± 0.00	-0.06 ± 1.98	28.59
	Cabauw soil, coupled	0.83 ± 0.00	-3.36 ± 1.85	29.96
Shortwave radiation [W/m^2]	Average soil, uncoupled, small	0.89 ± 0.00	16.02 ± 10.03	71.86
	Average soil, uncoupled	0.89 ± 0.00	1.87 ± 9.91	71.84
	Average soil, coupled	0.89 ± 0.00	1.51 ± 9.94	71.24
	Medium-fine soil, coupled	0.88 ± 0.00	0.55 ± 9.88	72.63
	Cabauw soil, coupled	0.89 ± 0.00	1.98 ± 9.93	71.77
Temperature [°C]	Average soil, uncoupled, small	0.95 ± 0.00	-0.15 ± 0.06	1.20
	Average soil, uncoupled	0.96 ± 0.00	-0.16 ± 0.06	1.18
	Average soil, coupled	0.96 ± 0.00	-0.23 ± 0.06	1.17
	Medium-fine soil, coupled	0.96 ± 0.00	-0.22 ± 0.06	1.15
	Cabauw soil, coupled	0.96 ± 0.00	-0.16 ± 0.06	1.17
Wind speed [m/s]	Average soil, uncoupled, small	0.96 ± 0.00	0.05 ± 0.07	1.12
	Average soil, uncoupled	0.96 ± 0.00	0.14 ± 0.07	1.13
	Average soil, coupled	0.96 ± 0.00	0.14 ± 0.07	1.11
	Medium-fine soil, coupled	0.96 ± 0.00	0.14 ± 0.07	1.12
	Cabauw soil, coupled	0.96 ± 0.00	0.15 ± 0.07	1.12

Table A2: *Statistics from winter runs (Jan-Mar 2019) in Cabauw for all settings.*

Variable	Setting	Correlation	Bias	RMSE
Humidity [g/kg]	Average soil, uncoupled, small	0.93 ± 0.00	-0.18 ± 0.03	0.68
	Average soil, uncoupled	0.93 ± 0.00	-0.15 ± 0.03	0.68
	Average soil, coupled	0.93 ± 0.00	-0.11 ± 0.03	0.67
	Medium-fine soil, coupled	0.94 ± 0.00	0.05 ± 0.03	0.63
	Cabauw soil, coupled	0.81 ± 0.00	-0.64 ± 0.03	1.23
Latent heat flux [W/m^2]	Average soil, uncoupled, small	0.92 ± 0.00	0.31 ± 5.11	48.47
	Average soil, uncoupled	0.93 ± 0.00	-2.39 ± 5.38	47.55
	Average soil, coupled	0.93 ± 0.00	-0.46 ± 5.38	47.60
	Medium-fine soil, coupled	0.93 ± 0.00	10.44 ± 5.66	46.71
	Cabauw soil, coupled	0.71 ± 0.01	-52.06 ± 4.48	103.19
Shortwave radiation [W/m^2]	Average soil, uncoupled, small	0.91 ± 0.00	31.55 ± 13.47	115.80
	Average soil, uncoupled	0.92 ± 0.00	23.23 ± 14.47	110.61
	Average soil, coupled	0.92 ± 0.00	19.44 ± 14.44	108.40
	Medium-fine soil, coupled	0.92 ± 0.00	21.29 ± 14.53	106.97
	Cabauw soil, coupled	0.91 ± 0.00	27.56 ± 15.76	117.22
Temperature [°C]	Average soil, uncoupled, small	0.97 ± 0.00	0.31 ± 0.07	1.23
	Average soil, uncoupled	0.97 ± 0.00	0.16 ± 0.08	1.11
	Average soil, coupled	0.97 ± 0.00	0.09 ± 0.08	1.08
	Medium-fine soil, coupled	0.97 ± 0.00	-0.03 ± 0.08	1.04
	Cabauw soil, coupled	0.96 ± 0.00	0.77 ± 0.09	1.76
Wind speed [m/s]	Average soil, uncoupled, small	0.92 ± 0.00	0.23 ± 0.05	1.13
	Average soil, uncoupled	0.92 ± 0.00	0.28 ± 0.05	1.13
	Average soil, coupled	0.91 ± 0.00	0.27 ± 0.05	1.14
	Medium-fine soil, coupled	0.92 ± 0.00	0.25 ± 0.05	1.12
	Cabauw soil, coupled	0.91 ± 0.00	0.37 ± 0.05	1.23

Table A3: *Statistics from summer runs (Jun-Aug 2019) in Cabauw for all settings.*

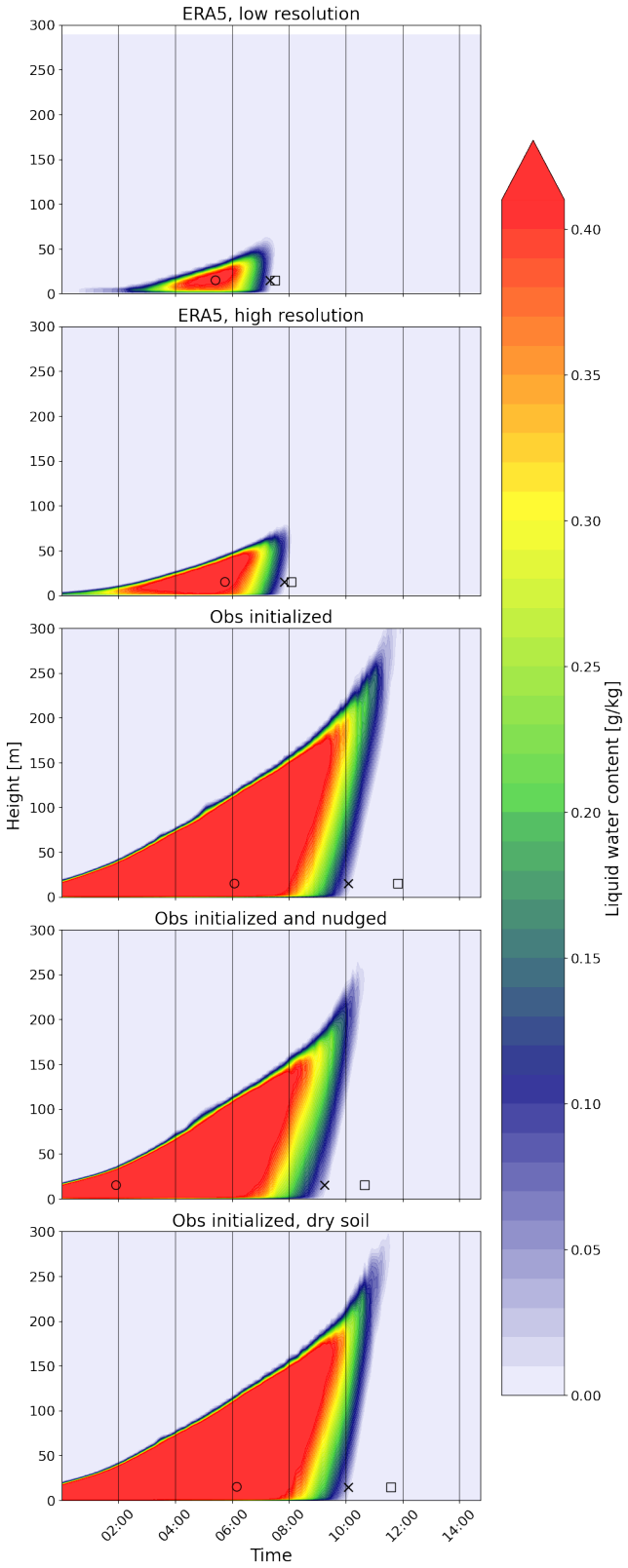

Figure A1: *Contour plots of liquid water content for the night of 22-23 March 2011. The circles, crosses and squares are the maximum, lifting and dissipation times, respectively.*